# Chapter 5

# EXPERMENTAL RESULTS AND DISCUSSION

## 5.1 Shock Wave Performance of Superfluid Shock Tube Facility

The superfluid shock tube facility has been developed as a versatile tool for general researches in low-temperature thermo-fluid dynamic phenomena. The shock tube was designed to be operated with the $HeII$-filled test section immersed in $HeII$. In this section, the general thermo-fluid dynamic performance test are conducted to verify the validity in wide range of experimental researches. The shock waves generated in the superfluid shock tube facility are investigated on the basis of the experimental results which are obtained at both room or cryogenic temperatures. The driver gas is helium gas and the driven gases are helium or nitrogen gas at both room temperature and cryogenic temperature.

### 5.1.1 Pressure history in gases

The pressure history in the shock tube are shown in Figures 5.1.1 - 5.1.1. The pressure is measured by the piezo-electric pressure transducers, which are fixed on the wall surface of the shock tube at 260 $mm$ (Transducer $A$ ) and 120 $mm$ ($B$) from the bottom of the test section. In these figures, the first pressure rise is measured by the transducer $A$, and the second one is measured by the transducer $B$, both of which are located in gas phase. The first pressure rise is resulted from the oncoming shock wave and the second is caused by a shock wave reflected at the bottom of the test section.

(a) Nitrogen (room and cryogenic temperature)

The typical pressure histories of the shock wave measured in the present shock tube are shown in Figure 5.1 and Figure 5.2. The driven gas is nitrogen gas in both cases. It is seen that the pressure behind the shock wave is kept almost constant. It may be concluded from the data that a shock wave is well formed in this facility in spite of using the *MO*-valve and of the bent tube in the low-pressure tube section. It should be, furthermore, added that the reproducibility is very good. In these figures the pressure level of the incident shock wave calculated from the *R-H-Gas* relation is also indicated by a dotted line. It is a general consequence in the shock tube theory that as the pressure ratio $p_{41}$ defined by $p_4/p_1$ between the pressure $p_4$ in high pressure chamber and the pressure $p_1$ in the low-pressure tube section becomes large, both the pressure rise at a shock and the shock Mach number $M_{SV}$ become large though they have limitations. Here $M_{SV}$ is the shock Mach number in the gas (vapor) phase, which is defined by $U_{SV}/a_1$ between the shock propagation speed $U_{SV}$ and the speed of sound $a_{1V}$ in the gas phase. It is seen from Figure 5.1 that the pressure rise behind a shock wave is quantitatively in good agreement with theoretical value in the present experiment. It is, however, seen from Figure 5.2 that in the case of very small $p_1$, the pressure rise due to a shock wave is much smaller than the theoretical value even at very large initial pressure ratio $p_{41}$. It may be the reason that the shock wave belongs to a low-density shock wave in the latter case.

The pressure history in the case of a shock wave propagating in saturated vapor of nitrogen is shown in Figure 5.3. It is seen that the pressure considerably decreases behind a shock wave with the lapse of time. It is well understood that when a shock wave propagates into gases with a strong positive density or negative temperature gradient in the direction of propagation, the pressure behind a shock wave gradually increases. In fact, shown in Figure 5.3 is not the case. This may be caused due to the condensation of compressed vapor on the free surface or on the cryogenic shock tube wall behind a shock wave. When a shock wave propagates into gas phase, the pressure and temperature behind a shock wave drastically increase, but the temperature of gas in the vicinity of a cooled shock tube wall or a free surface can not follow this increase. Accordingly, the gas in the vicinity of

the cooled tube wall will condense there, which leads to pressure decrease behind an incident shock wave.

(b) Helium (room and cryogenic temperature)

Figure 5.4 shows the similar results in the case that the driven gas is at room temperature helium gas. In this case the pressure rise is considerably small and the pressure rise is slow compared with the case of nitrogen gas in the same condition, $p_4$ and $p_1$, as shown in Figure 5.4. In this case a shock wave is, in fact, not formed. It is found that in the case of helium gas in the low-pressure tube section a shock wave is hardly formed if the initial pressure ratio $p_{41}$ is less than about 8. Figure 5.5 shows the result in the case that the initial pressure ratio is very large. The pressure rise deviates downwards from the theoretical value because of a low-density shock wave as in the case of Figure 5.5.

The result of a shock wave propagating into saturated helium vapor with $HeII$ in the test section is shown in Figure 5.6. The pressure behind the shock wave in the vapor phase is not constant but gradually increases as the result of a strong negative temperature gradient in the cryogenic shock tube. The cryogenic shock tube is inserted in the cryostat and thus the vapor as the driven gas has a strong temperature gradient, that is to say 300 $K$ at the entrance to the cryostat portion, about 80 $K$ around the top portion of the cryostat portion and down to 2 $K$ near the free surface of $HeII$ in the case of $HeII$ operation. This result may be quite different from that in the case of nitrogen vapor where the most part of the cryogenic portion is maintained at the temperature of liquid nitrogen, about 80 $K$. Accordingly, the temperature of the tube wall where the pressure transducer is mounted is higher than that near the $HeII$ free surface and the pressure rise due to the shock wave compression will not cause condensation of the helium vapor on the shock tube wall. It is the reason that the temperature behind the shock wave increases toward upstream. Thus the pressure does not decrease behind a shock wave in this case.

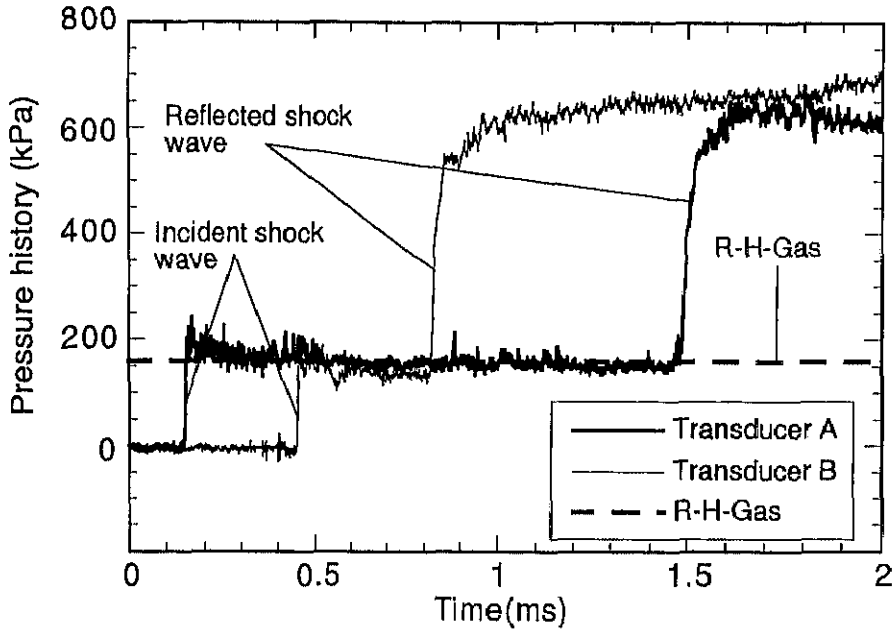


Figure 5.1: Pressure history of typical shock wave. (driver gas; helium, driven gas; nitrogen) $p_4 = 425.5\ kPa$, $p_1 = 53.50\ kPa$, $p_{41} = 7.95$, $U_{SV} = 664\ m/s$, $M_{SV} = 1.90$, Both gases at 293 $K$

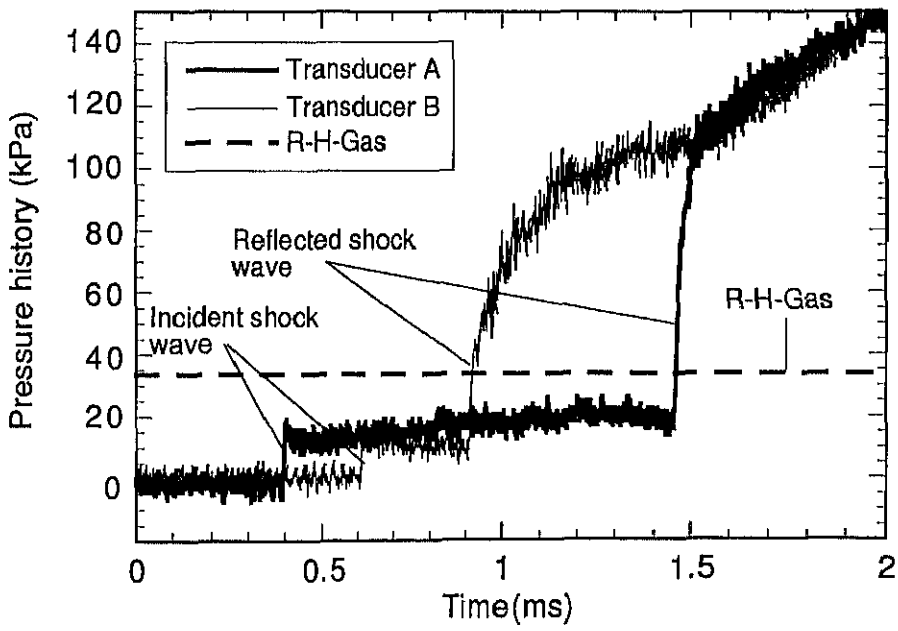


Figure 5.2: Pressure history of typical shock wave. (driver gas; helium, driven gas; nitrogen) $p_4 = 425.5\ kPa$, $p_1 = 1.50\ kPa$, $p_{41} = 278.14$, $U_{SV} = 934\ m/s$, $M_{SV} = 2.67$, Both gases at 293 $K$

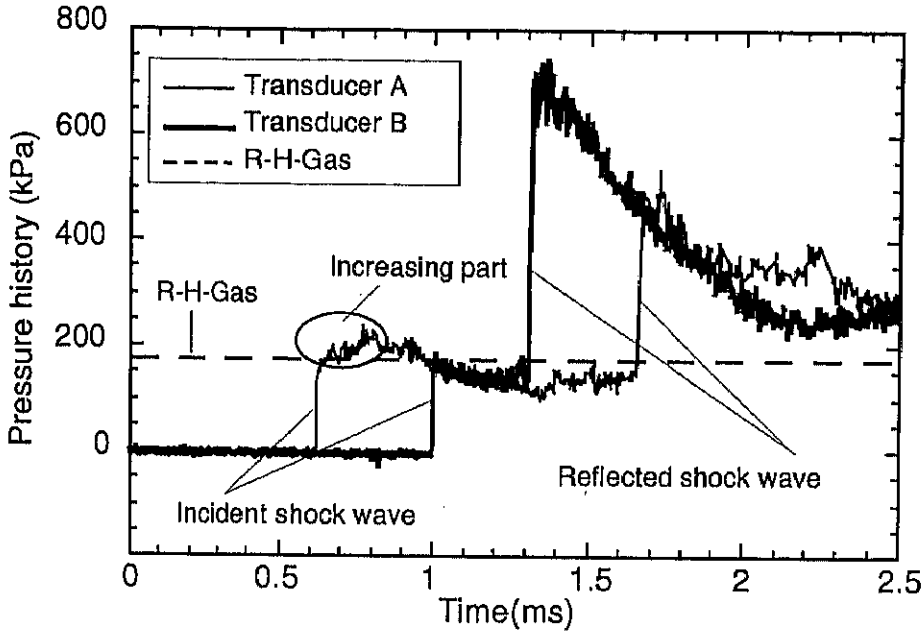


Figure 5.3: Pressure history in the case of saturated nitrogen vapor 77 $K$ in the low-pressure tube section. (driver gas; helium, driven gas; nitrogen) $p_4 = 425.5\ kPa$, $p_1 = 19.50\ kPa$, $p_{41} = 21.81$, $U_{SL} = 529\ m/s$, $M_{SV} = 3.02$

### 5.1.2 Performance of initial pressure ratio

Figure 5.7, Figure 5.8, Figure 5.9 and Figure 5.10 show the fundamental shock wave performance of the superfluid shock tube facility. All these results are shown as a function of the initial pressure ratio $p_{41}$, which is defined as the pressure ratio of the pressure in the driver section to that in the driven section, $p_{41} = p_4/p_1$. The impinging shock Mach number $M_{SV}$ is plotted against $p_{41}$ in Figure 5.7, the pressure jump of impinging shock wave $p_{21} = p_2/p_1$ in Figure 5.8, the shock Mach number $M_{SL}$ in $HeII$ in Figure 5.9 and the pressure jump of transmitted compression shock wave $\Delta P$ in Figure 5.10. The magnitudes of $M_{SV}$ and $M_{SL}$ are considered to be the indices of the intensity of shock wave. In these figures, the solid lines in Figure 5.7 and Figure 5.8 are the theoretical curve calculated on the basis of the simple shock tube theory, Rankine-Hugoniot ($R$-$H$-$Gas$) relation, and the solid lines in Figure 5.9 and Figure 5.10 are just guide lines for each temperature. It is noted in the Figure 5.7 and Figure 5.8 that the variations of $M_{SV}$ and $p_{21}$ with $p_{41}$ hardly agree with the $R$-$H$-$Gas$ curve. They are much smaller than the theoretical predictions, approximately half to one

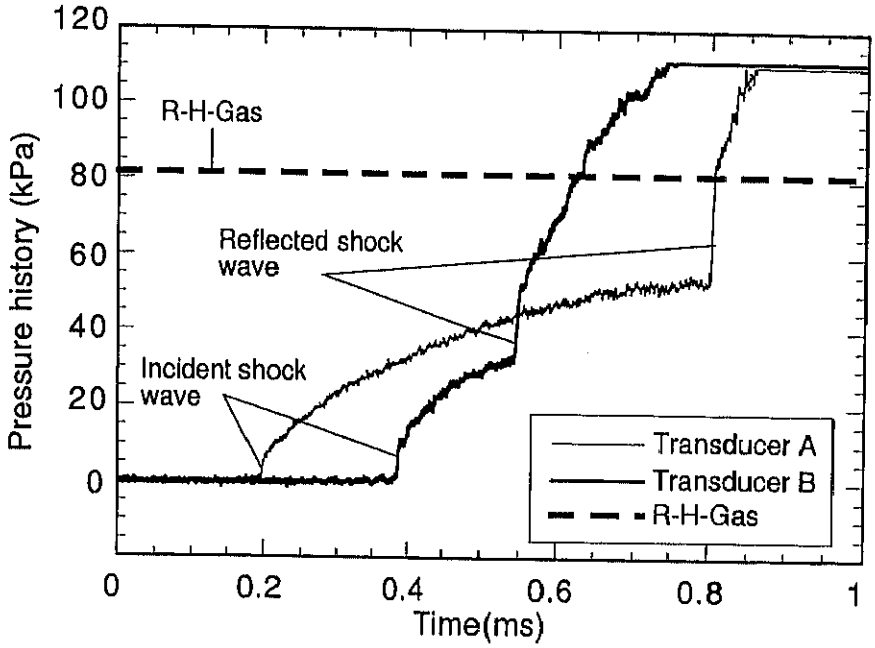


Figure 5.4: Pressure history in the case of helium gas. (driver gas; helium, driven gas; helium) $p_4 = 425.5\ kPa$, $p_1 = 53.5\ kPa$, $p_{41} = 7.95$, $U_{SL} = 1060\ m/s$, $M_{SV} = 1.05$, Both gases at 293 $K$

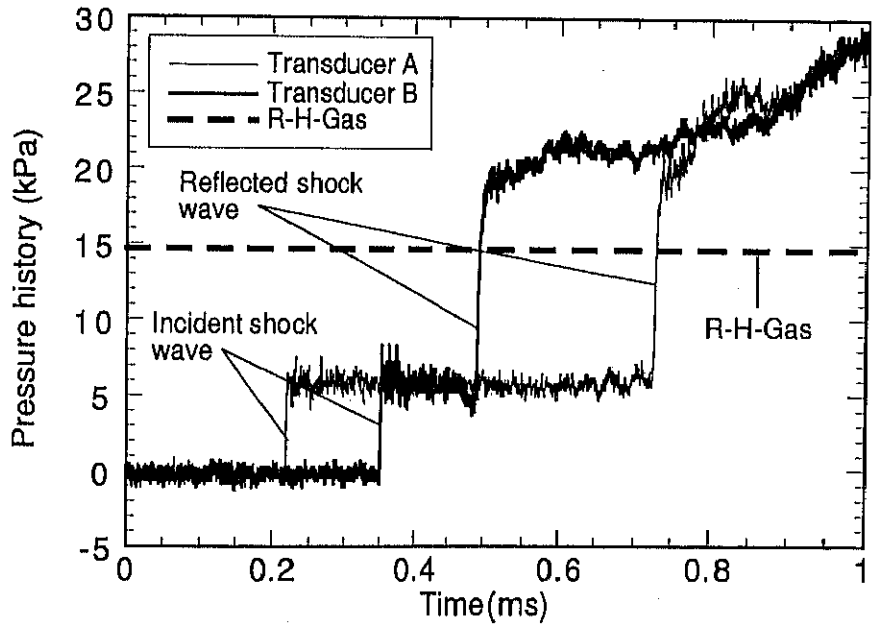


Figure 5.5: Pressure history in the case of helium gas. (driver gas; helium, driven gas; helium) $p_4 = 425.5\ kPa$, $p_1 = 2.66\ kPa$, $p_{41} = 159.6$, $U_{SL} = 1520\ m/s$, $M_{SV} = 1.51$, Both gases at 293 $K$

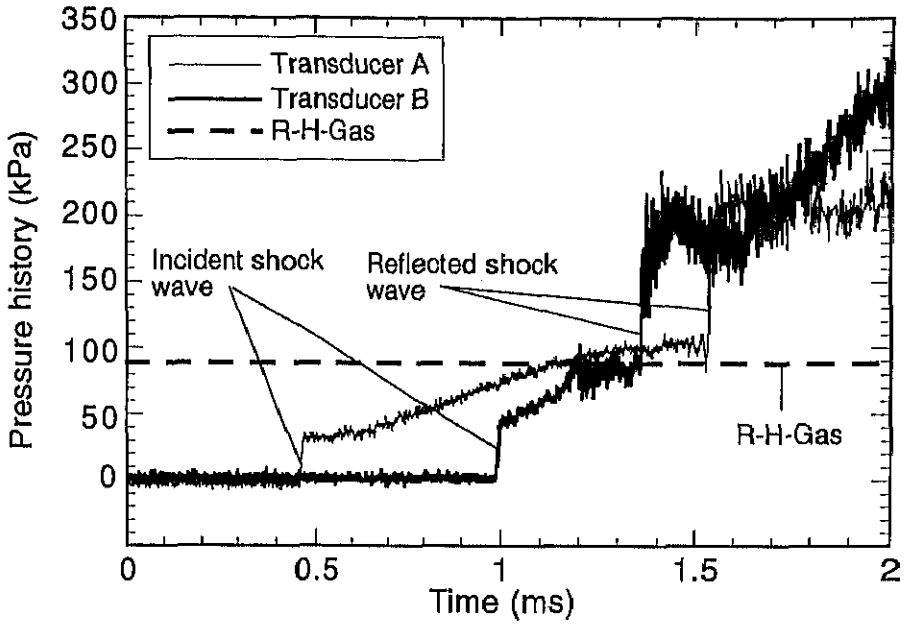


Figure 5.6: Pressure history in the case of saturated helium vapor at $2K$ in the low-pressure tube section. (driver gas; helium, driven gas; helium) $p_4 = 567.4\ kPa$, $p_1 = 2.06\ kPa$, $p_{41} = 274.6$, $U_{SL}$= 373 $m/s$, $M_{SV} = 4.66$

third of the theoretical one. This fact seems to suggest that the shock wave still has not been fully developed at the moment it reaches the test section.

It should also be taken into account that the opening time of a diaphragm-free shock tube is generally longer than that of a diaphragm-type shock tube, and some reflection or diffraction may occur in the bent tube portion and the conversion section from a circular cross section to a rectangular one in the present shock tube. Accordingly, the impinging shock Mach number $M_{SV}$ and pressure jump $p_{21}$ are less than the theoretical prediction based on $p_{41}$. It is, however, required in practical application of the facility to predict the quantities of $M_{SV}$ and $p_{21}$. On the other hand, it is noted in Figure 5.11 that the relation between $p_{21}$ and $M_{SV}$ is in good agreement with the theoretical curve. This implies that the shock waves generated in this shock tube satisfy the gasdynamic shock wave condition. This means every jump quantity can be estimated with the aid of the shock condition provided that $p_2$ is measured. It is seen in the Figure 5.9 and Figure 5.10 that the transmitted shock Mach number $M_{SL}$ and the pressure jump $\Delta p$ in the $HeII$ almost linearly increases with $p_{41}$. The transmitted compression shock waves propagate at a shock Mach number about 1.00 $\sim$ 1.15, which

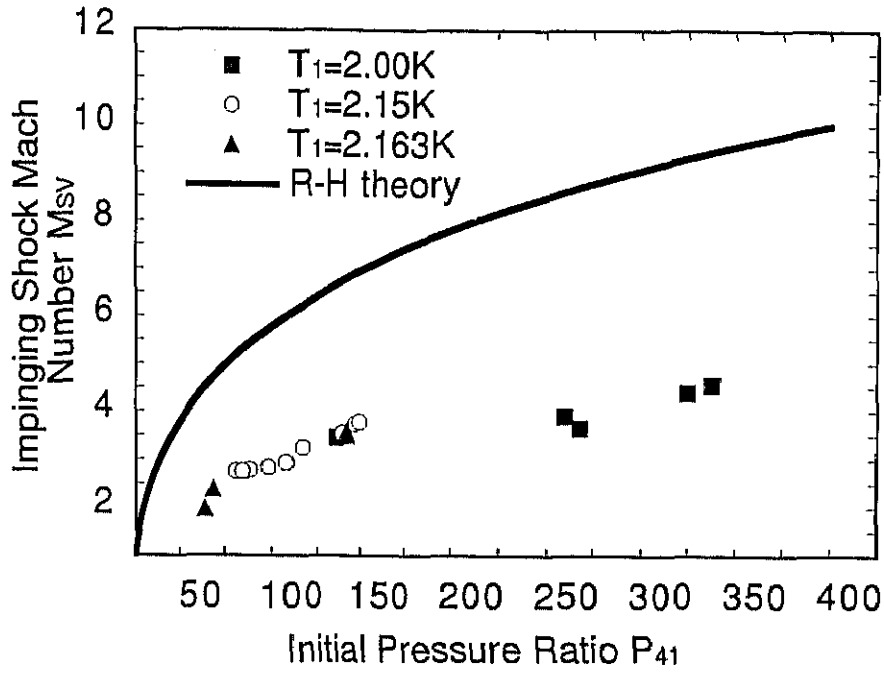


Figure 5.7: Shock wave performance of superfluid shock tube facility. $p_{41}$ *vs.* $M_{SV}$; $M_{SV}$ = impinging shock Mach number in the vapor. $p_{41} = p_4/p_1$, $p_4$ = pressure of high-pressure helium in the driver section. $p_1$ = initial pressure of saturated helium vapor in the driven section.

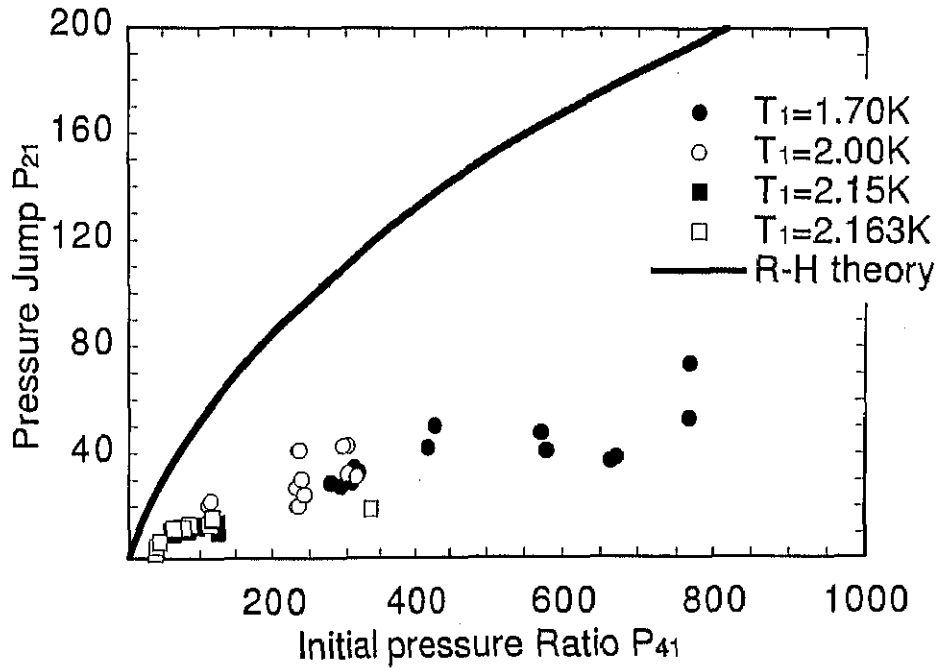


Figure 5.8: Shock wave performance of superfluid shock tube facility. $p_{41}$ *vs.* pressure jump $p_{21}$; $p_{21} = p_2/p_1$, $p_2$ = wave front pressure of impinging shock wave in the vapor.

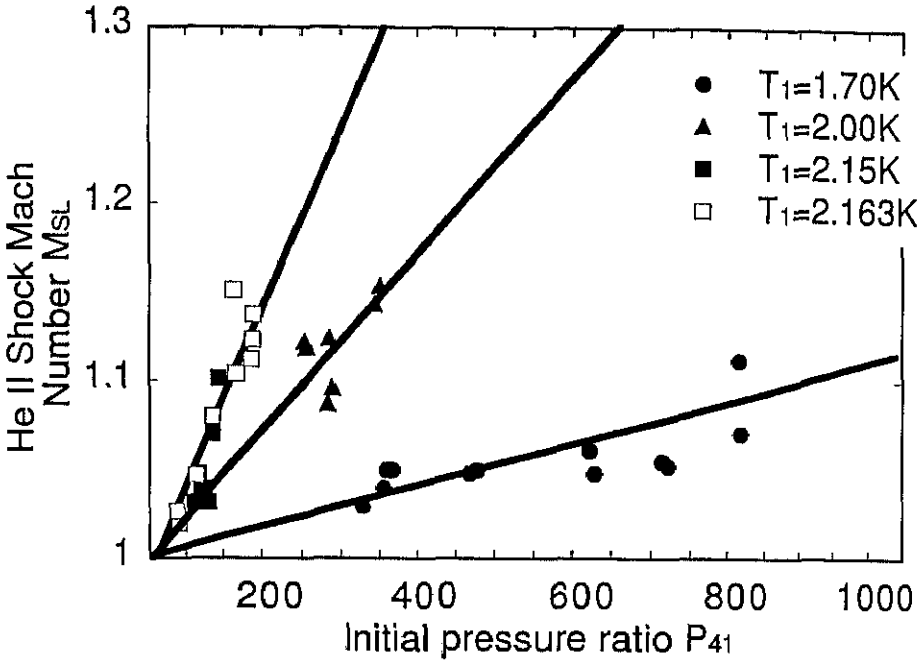


Figure 5.9: Shock wave performance of superfluid shock tube facility. $p_{41}$ *vs.* $M_{SL}$; $M_{SL}$ = Shock Mach number of transmitted compression shock wave in *HeII*.

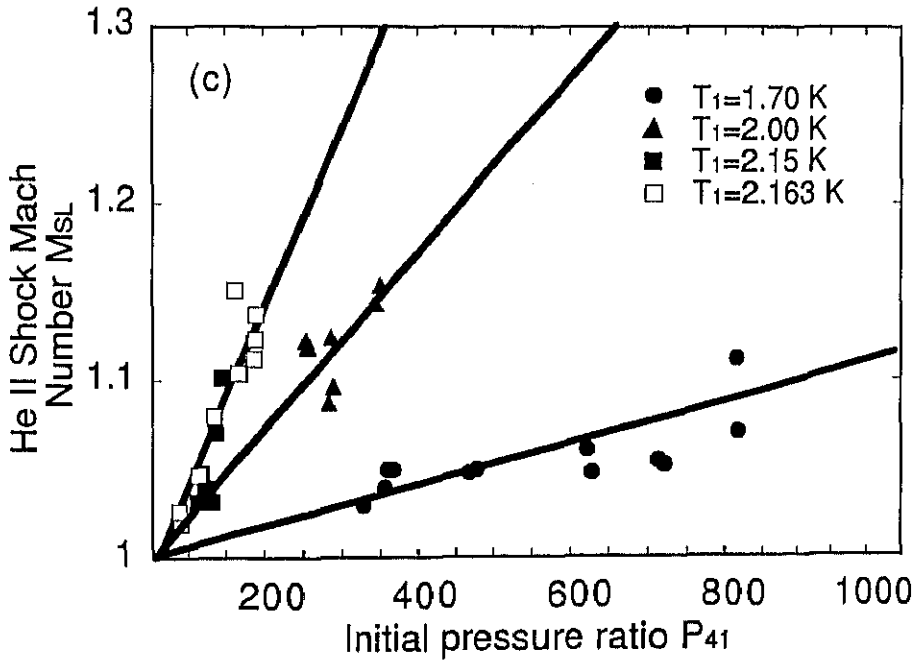


Figure 5.10: Shock wave performance of superfluid shock tube facility. $p_{41}$ *vs.* $\Delta p$ in *HeII* ; $\Delta p$ = pressure jump of transmitted compression shock wave in *HeII*.

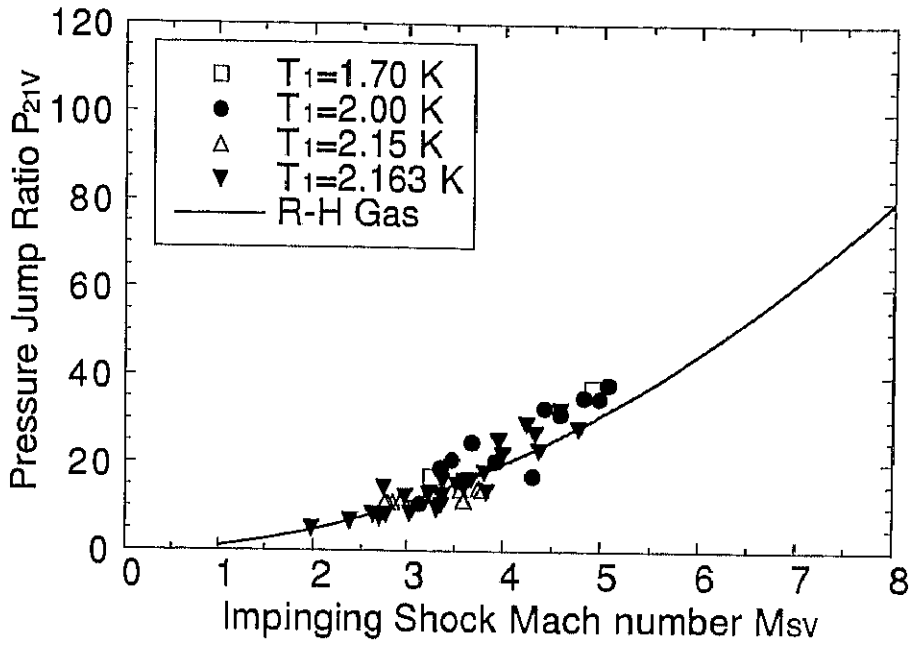


Figure 5.11: Impinging shock wave condition in the helium vapor. $p_{21}$ *vs.* $M_{SV}$ Solid line is the Rankine-Hugoniot relation (*R-H-Gas*).

indicates they are rather strong shock waves in liquids. The dependence on the bath temperature is clearly evident within the measurement accuracy of this experiment.

## 5.2 Propagating Shock Wave in Cryogenic Shock Tube

### 5.2.1 Typical example of detected signals

A typical example of the time records of the detected signals, by the pressure transducers $B$ and $C$, the superconductive temperature sensor and the photo diode is shown in Figure 5.12. All the detectors are located in the order of shock wave propagation as mentioned above. Laser beam passes through the test section at the distance of 30 $mm$ measured from the bottom and the superconductive temperature sensor is located in the $HeII$ in the test section at 35.5 $mm$ from the bottom and the $HeII$ free surface is situated at 65 $mm$ from the bottom in this particular run. In fact the temperature of the driven gas varies in a wide range from 80 $K$ at the top of the cryogenic section down to about 2 $K$, and the temperature is 1.90 $K$ only on the free surface. The shock wave signal is first detected by the transducer $B$ in the vapor as indicated by the trace (a) in Figure 5.12. A sharp pressure jump at the wave front of the incident shock is clearly recorded. The second. third and fourth signals are detected by the pressure transducer $C$ by the trace (b) , the superconductive temperature sensor by the trace (c) and the photo diode by the trace (d) all in $HeII$, respectively. The pressure behind the incident gasdynamic shock wave gradually increases owing to the strong temperature gradient developed from the initial temperature gradient in the low-pressure shock tube section, from 300 $K$ down to about 2 $K$. The transducer $C$ detects the arrival of a transmitted compression wave propagating through $HeII$. This pressure rise seems very sharp unlike compression waves in ordinary liquids. The reason for this is that $HeII$ has considerably higher compressibility than any other liquids to result in better impedance matching for a pressure wave transmission through a gas-liquid $HeII$ interface. This means that a gasdynamic shock wave is transmitted much more efficiently into $HeII$ than into any ordinary liquids. This property is quite desirable to generate a shock wave in $HeII$ by impinging a gasdynamic shock wave on a $HeII$ free surface. The arrival of the transmitted shock wave is recorded even with the superconductive temperature sensor as a negative temperature jump as small as about several $mK$, as seen from the trace (c). Finally, the shock wave is detected by the photo diode as indicated by the trace (d). Then, the

shock wave is reflected from the bottom of the shock tube. The signal from the reflected wave cannot be identified from the photo diode signal, but is recorded as the second negative temperature jump by about several $mK$ on the superconductive sensor trace (c). It is also recorded as a second large pressure jump on the pressure sensor trace (b). As seen from these signals the reflected wave in $HeII$ from the solid boundary is still a compression wave. Some other wave signals are also recorded on the traces in Figure 5.12. The second (positive) vapor pressure jump of the trace (a) results from a reflected gasdynamic shock wave from the $HeII$ free surface. It is interesting to note that the third pressure rise is caused by the penetration of a $HeII$ shock wave through the $HeII$-vapor interface into vapor phase, which is reflected from the tube bottom. The large spiky temperature rise, as large as 100 $mK$, seen on the trace (c) results from a thermal shock wave which propagates much slower than a compression $HeII$ shock wave through. The detail will be described later.

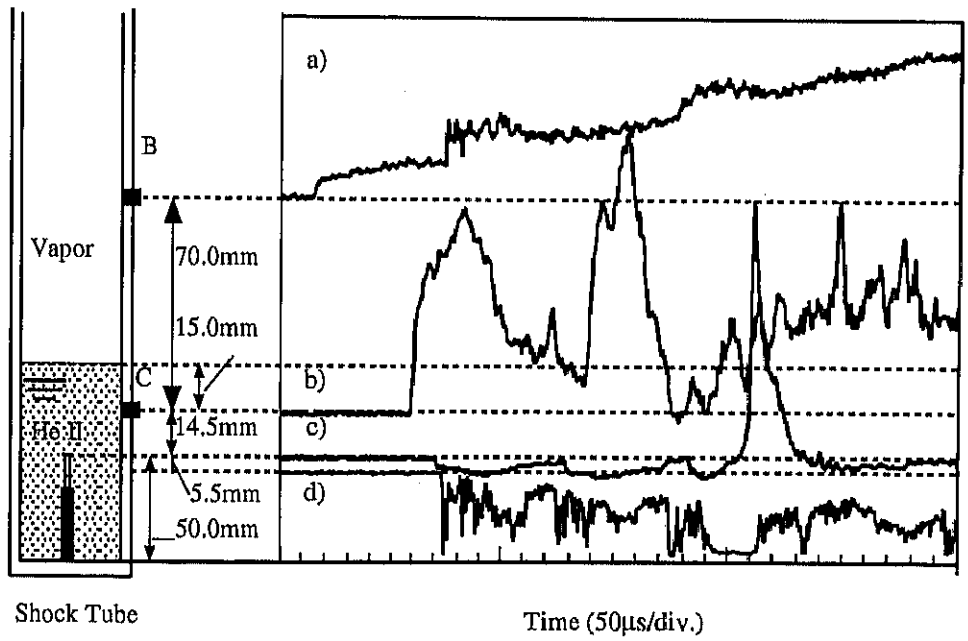


Figure 5.12: Typical example of time variation of detected signals. Driver gas; $p_4 = 660$ $kPa$ (300 $K$), driven gas; saturated vapor of $HeII$ $p_1 = 2.20$ $kPa$ ($T_1 = 1.90$ $K$), $p_{41} = 300$. Incident shock speed = 307 $m/s$, shock Mach number $M_{SV} = 3.86$. Transmitted shock speed in $HeII$ = 252 $m/s$, transmitted shock Mach number $M_{SL}$ =1.05. Detected signals are: a) from pressure transducer $B$, b) from pressure transducer $C$, c) from superconductive temperature sensor and d) from photo diode.

### 5.2.2 Pressure variation in propagating shock wave

The transient variations of the pressure of a propagating shock wave in the cryogenic shock tube are shown in Figure 5.13, which are measured by the pressure transducers installed on the wall surface in the vapor phase (a, b, c) and in the *HeII* phase (d, e), respectively. These are not representative of a single shock wave data point but of several individual data points, because of satisfactory reproducibility among the data points. We focus on the pressure profile measured in the vicinity of the *HeII* free surface. The trace (a) and (b) are detected by transducers located in the helium vapor and the trace (c) is measured in the vapor phase in the vicinity of the *HeII* free surface. The trace (d) and (e) are the pressure histories in *HeII*. The first and second stepwise pressure rises of (a) result from the arrivals of an impinging shock and a reflected one from the *HeII* free surface. It seems that the reflection is similar to that obtained from the solid boundaries. It is, however, noted in trace (b) that the second large pressure jump which results from the shock reflection from the *HeII* free surface is highly unstable. In the data trace (c), which is measured closer to the free surface, the reflected shock wave shows a very large amplitude, which is considerably different from reflected shocks from the solid boundaries. In traces (d) and (e), the pressure jumps from the transmitted compression shock wave and the reflected shock wave from the bottom of the test section, which is the second jump in (e). The pressure jump $\Delta p$ in *HeII* is also very large as observed in the case of (c). From the visualization photograph, one observes a transmitted compression shock wave, accompanied with a fluctuating density state behind it and a thickened free surface region.

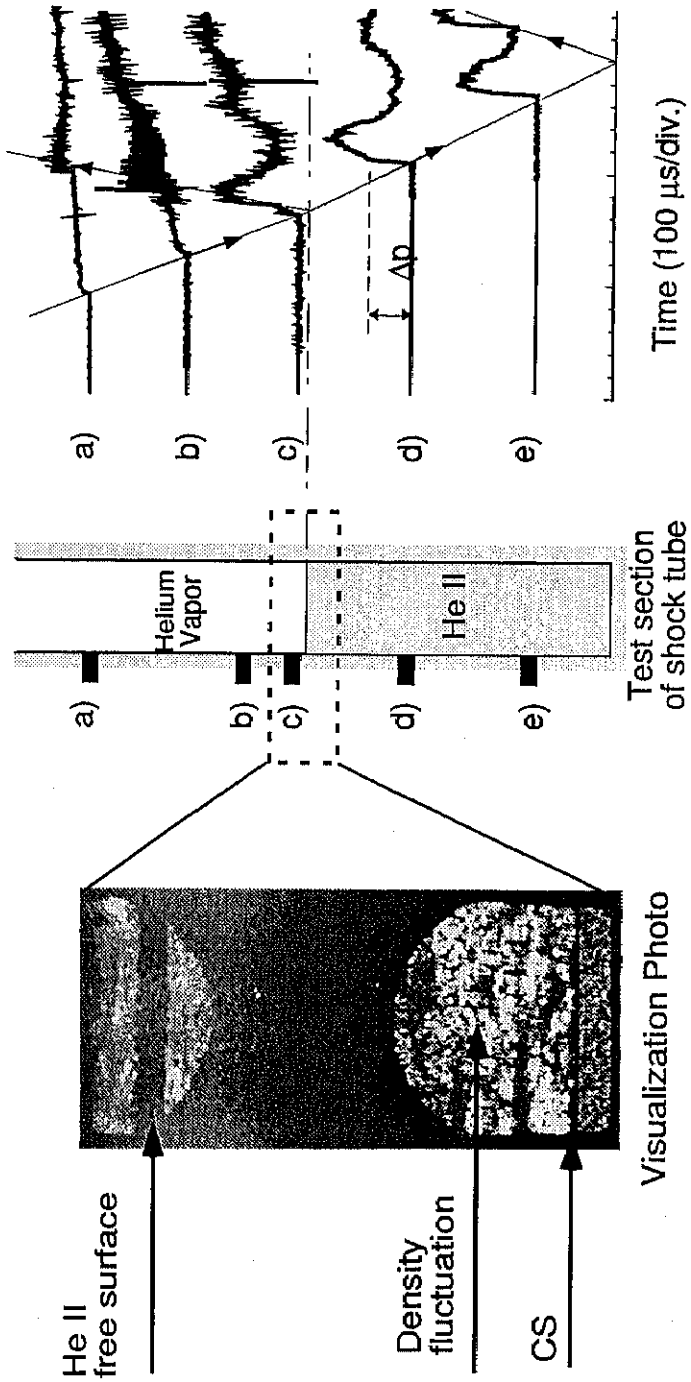


Figure 5.13: Pressure variations associated with the propagating shock waves. a), b), c) measured in helium vapor and d), e) measured in *HeII*. $p_1 = 18.1\ torr$, $T_1 = 2.00\ K$, $U_{SV} = 327.7\ m/s$, $M_{SL} = 1.09$, $U_{SL} = 249.1\ m/s$. *CS*: Transmitted compression shock wave.

## 5.3 Transmitted Compression Shock Wave in Superfluid Helium

*HeII* is expected to be an excellent coolant for cooling of superconductive magnets and space devices which require low-temperature environment for high performance. A deep understanding not only of steady *HeII* heat transfer but also of transient heat transfer is needed for further promotion of the practical applications of *HeII* to cryogenic cooling. The quench mechanism of a *HeII* cooled superconductive magnet involving a violent pressure oscillation and boiling heat transfer is not fully understood even now. Most studies of *HeII* have focused on thermal shock waves, which is peculiar physical phenomena in *HeII*, but quite a few have been interested in compression shock waves. However, if we consider the problems of highly transient heat transfer in *HeII* in which strong non-linearity dominates, we understand that the non-linearity not only of a thermal shock wave but of a compression shock wave must be taken into account. This is one of the motivation for the present study of the non-linearity of a compression shock wave propagating through *HeII*.

It is usually very difficult to quantitatively describe shock wave propagation through liquid. This is not only because the total account of available data are rather scarce owing to the difficulty in experiments, but because ordinary liquids do not have high compressibility like gases and thus strong shock waves are hardly generated in liquid and the dynamic nature is not fully described on the basis of the straightforward extension of gasdynamic theory. However, *HeII* has a very large compressibility compared with other liquids and consequently a clear shock wave can easily been observed. And the behavior can be well described by the two-fluid equation. This has been verified by the experimental results on thermal shock waves.

In this section, the Numerical solution to Rankine-Hugoniot relation in *HeII* will be compared with the present experimental results on a compression shock wave.

### 5.3.1 Propagation speed

The propagation speed of the transmitted compression shock wave, which is represented in the form of $U_{RL}/U_{SL}$, is plotted against the shock Mach number $M_{SL}$ in Figure 5.14. Here $U_{SL}$ is the transmitted compression (incident) shock speed and $U_{RL}$ is the reflected compression (reflected) shock speed from the shock tube bottom. The solid line is the *R-H-Gas* relation in the case of the gas dynamics shock wave reflected from rigid wall. The propagation speed of reflected shock wave from a rigid wall is generally slower than that of incident shock understood from the *R-H-Gas* relation for gas phase. However, it is found in the result in *HeII* that the propagation speed of the reflected shock wave becomes faster than that of incident shock wave. It may seem that the shock waves become strong after reflection from the shock bottom. However, in fact the reflected shock Mach number $M_{RL}$ decreases. The reflected shock wave ($M_{RL}$ =1.00, $U_{RL} = a_2$ = 270 $m/s$) propagates almost at the speed of sound though the incident shock Mach number $M_{SL}$ slightly exceeds unity ($M_{SL}$ = 1.00 $\sim$ 1.15, $U_{SL}$ = 250 $m/s$). In the compressed region, the speed of sound becomes large compared with that in saturated vapor pressure as seen from Figure 5.15. Accordingly, the propagation speed of the reflected shock wave increases though the reflected shock Mach number decreases upon the reflection from the shock tube bottom.

### 5.3.2 Pressure jump

The pressure jump data of the transmitted compression shock wave, $\Delta p/p_1$, is plotted against the shock Mach number $M_{SL}$ in Figure 5.16. Here $a_{1L}$ is the speed of the first sound before the arrival of a shock wave. And $p_1$ is the initial (upstream) pressure of *HeII*, equal to the saturated vapor pressure at the temperature $T_1$, and $\Delta P$ is the pressure jump across a compression shock wave. In this figure, the solid lines are the theoretical lines of Khalatnikov's approximation for a compression shock in *HeII*, which is a weak shock wave approximation derived through neglecting terms higher than the second order of smallness relative to pressure jump $\Delta p$ as described in chapter 2 (p20) . The dotted line is the numerical solution calculated from the *R-H-HeII* relation for *HeII* described according to the two-fluid model.

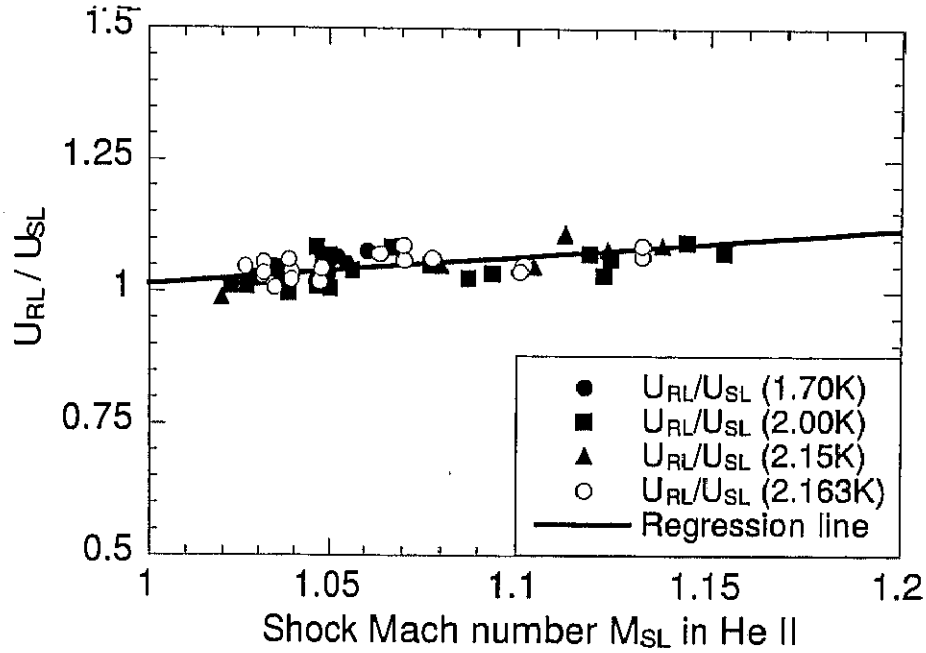


Figure 5.14: $U_{RL}/U_{SL}$ versus Transmitted shock Mach number $M_{SL}$. $U_{SL}$ is the incident shock speed and $U_{RL}$ is the reflected shock speed.

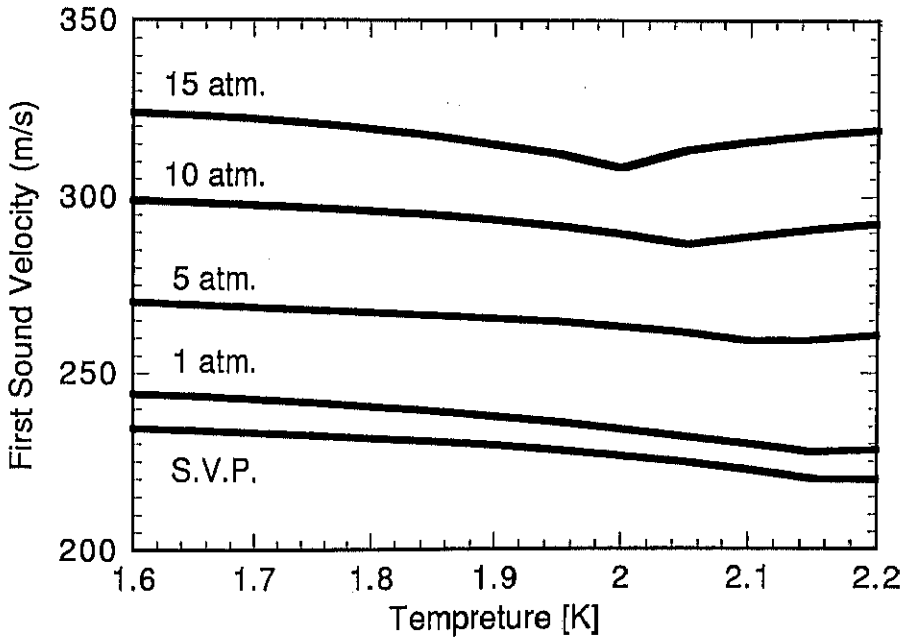


Figure 5.15: Dependence of first-sound velocity on temperature and pressure. *S.V.P.* is the saturated vapor pressure.

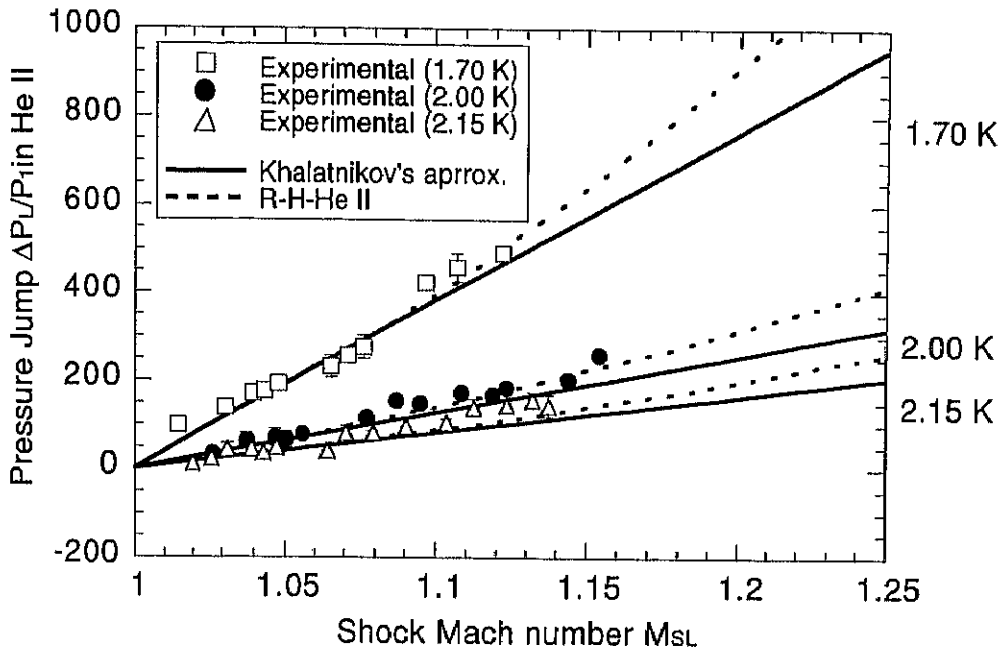


Figure 5.16: Pressure jump $\Delta p$ result at the wave front of the transmitted compression shock wave in $HeII$ as a function of shock Mach number $M_{SL}$. The dotted lines are *R-H-HeII* curves. The solid lines are Khalatnikov's approximation. $\Delta P_L$ = Pressure jump of transmitted compression shock wave at the shock front in $HeII$. $M_{SL} = U_{SL}/a_{L1}$; $U_{SL}$ = Transmitted compression shock wave speed in $HeII$. $a_{L1}$ = First sound sped in initial quiescent $HeII$.

It is seen from Figure 5.16 that the numerical solution and Khalatnikov's approximation coincide with each other as $M_{SL} \to 1$, but at higher Mach numbers Khalatnikov's approximation underestimates the pressure jump. The reason for this is that the non-linearity appears as $M_{SL}$ increases in compression shock waves in $HeII$ . The experimental data points are in good agreement with the *R-H-HeII* relation.

### 5.3.3 Temperature jump

The temperature jump data, $\Delta T\ /T_1$, for the compression shock wave is plotted as a function of $M_{SL}$ in Figure 5.17. It is noted that the compression shock process in $HeII$ is regarded as an isothermal one in Khalatnikov's theory, that is $\Delta T = 0$. However the experimental data points and the *R-H-HeII* relation indicate an obvious temperature decrease in the process. The magnitude of $\Delta T$ even increases with the wave strength $M_{SL}$. The temperature drop in compression shocks in $HeII$ results from the negative thermal

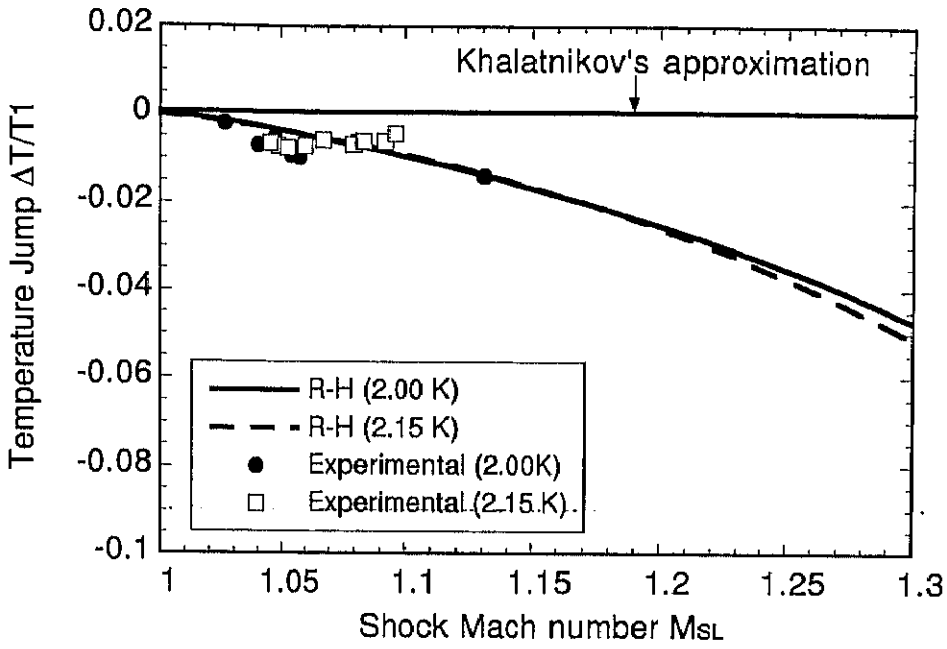


Figure 5.17: Variation of the temperature jump $\Delta T$ at the wave front of the transmitted compression shock wave with the shock Mach number $M_{SL}$. The solid and dotted lines are the numerical calculation results based on *R-H-HeII* relation for $T_1 = 2.00\ K$ and 2.15 $K$, and Khalatnikov's approximation result, that is $\Delta T = 0$.

expansion coefficient of *HeII*, which is the very characteristics of compression shock waves in *HeII*. The temperature decrease of the experimental data points are in good agreement with the *R-H-HeII* relation.

It is reasonable to consider that the experimental results is in good agreement with the *R-H-HeII* relation of numerical solution. However, it has been sometimes reported that experimental data hardly agrees with the *R-H* relation in such conventional liquids as water. Accordingly, it is rather a surprising result that the experimental data are in good agreement with the theoretical result for superfluid liquid helium. Of course, this good agreement should be primarily attributed to the fact that *HeII* has high compressibility, which results in good matching in the shock impedance between *HeII* and helium vapor. On the other hand, it may be considered to suggest the excellence in the performance of the present experimental facility. Now that it is experimentally verified that the transmitted compression shock waves quite well obey the *R-H-HeII* relation, the flow velocity and the counter flow velocity behind a compression shock wave, which are very

difficult to be measured in experiments, can be derived from the *R-H-HeII* relation provided that such physical quantities as the temperature and the pressure are given. The results are shown later.

### 5.3.4 Visualization result

The visualization photographs of a propagating transmitted compression shock wave in *HeII* are shown in Figure 5.18 (a) through (e). These may be regarded as a series of compression shock wave (*CS*) evolution because of excellent reproducibility, though these picture are not provided from a single shock wave event but are composed of several independent shots. In a Schlieren photograph, a compression shock wave appears as a single line. The compression shock wave propagates downward in the shock tube as seen in Figure 5.18 (a) $\sim$ (d). In the photo (d), the compression shock wave has already gone downward out of view. The photo (e) detects the reflected compression shock wave (*CR*) from the shock tube bottom. It is of interest to note that in the region behind the shock wave the density is highly disturbed. The reason for the disturbance has not been made clear at this time because of the visualization method yields only instantaneous information.

In order to investigate the time variation of thermodynamic state behind a transmitted compression shock wave in *HeII*, the measurement of laser beam transmission through *HeII* is applied. When the density of fluid changes, the refractive index also changes, which causes some deflection of laser beam through the fluid Laser beam is introduced into the test section of the shock tube through the optical windows, and the intensity is detected by a *PIN* photo diode at the opposite side outside of the cryostat. Such a variation in the physical property as the density of the fluid causes the deflection and scattering of the laser beam, which results in drop in the output signal from the photo detector.

Figure 5.19 shows both measurement results and the corresponding photographs. Figure 5.19(a) does the case of *HeII* and (b) shows the case of liquid nitrogen ($LN_2$). In Figure 5.19, one sees two sharp drops, which are the signals of the arrivals of the incident and the reflected shocks, respectively. In the case of *HeII* shown in Figure 5.19(a), there are many large scale fluctuation peaks in addition to two major shock signals of the arrivals

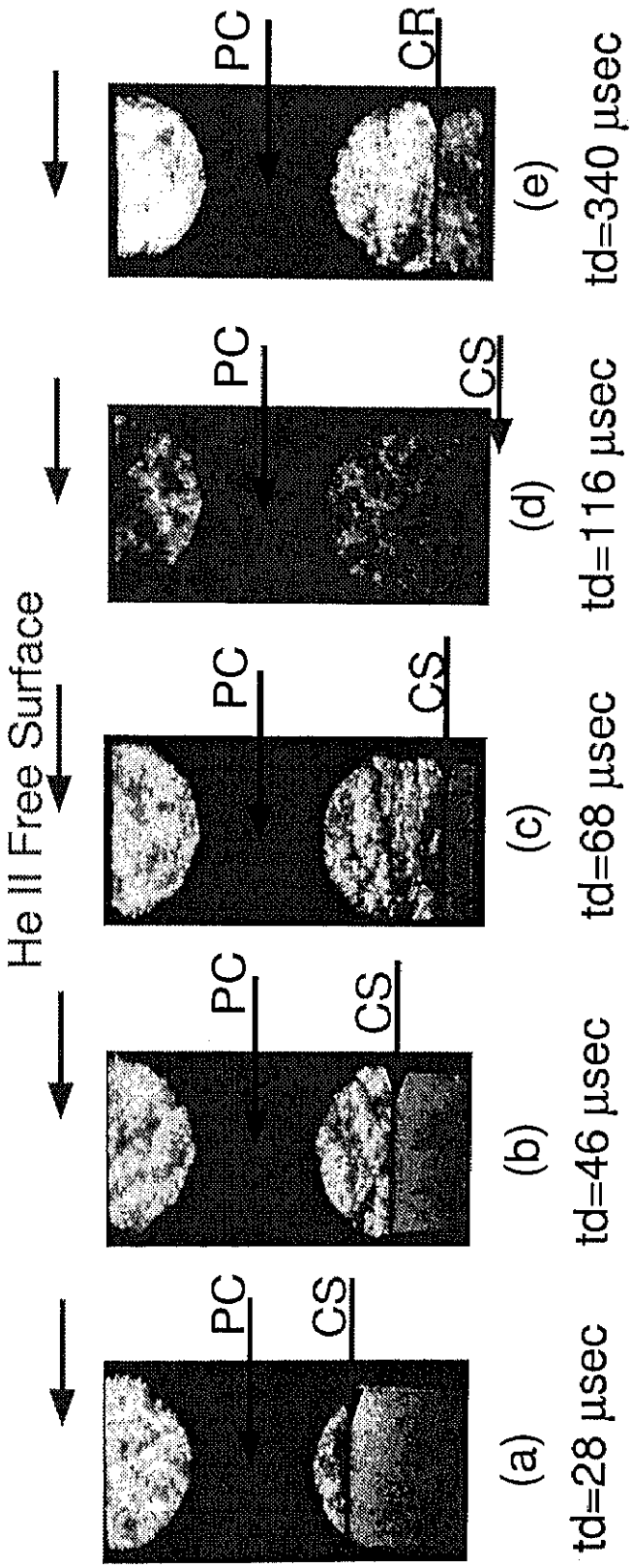


Figure 5.18: Visualization photograph of propagating transmitted compression shock wave in $HeII$. The quantity $t_D$ is the time delay of photographing from signal detection by the pressure transducer C ($PC$), which is equipped between the upper and lower windows. CS: Compression shock wave. CR: Reflected compression shock wave. (a) $t_D = 28$ $\mu$ sec, (b) $t_D = 46$ $\mu$ sec, (c) $t_D = 68$ $\mu$ sec, (d) $t_D = 116$ $\mu$ sec, (e) $t_D = 340$ $\mu$ sec

of the incident and the reflected shocks. It seems that the large-scale fluctuation with gradual decay corresponds to the density fluctuation behind a transmitted shock seen in the visualization result. They generated as a result of shock compression, through the detail of the generation is not made clear at this stage of research.

On the other hand, in the case of Figure 5.19(b), only two sharp drops are seen. The compression shock wave in $LN_2$ has already gone downward out of view in Figure 5.19(b) because the shock speed in $LN_2$ is greater than that in $HeII$. There are several weak pressure waves reflected from projections on the shock tube wall such as the pressure transducers equipped on the shock tube wall and the window frames. However the major density changes are only induced by the main shock wave, and there is no large-scale fluctuation. This result is consistent with the visualization result, but apparently differents from the case of $HeII$. The reason why the fluctuation occurs in $HeII$ is not yet fully understood. However, from the result of Figure 5.19, it is considered as follows; The thermodynamic state of the free surface in the moment of the gasdynamic shock impingement is apparently different from that of the liquid nitrogen, for example, in the case of $HeII$, the thermodynamic state near the free surface is over the critical pressure in Figure 5.20. In contrary, in the case of liquid nitrogen similar shock compression results in sub-critical pressure, shown in Figure 5.21. So it is diduced that the thermodynamic state of the free surface caused the fluctuation behind the compression shock wave in $HeII$. Furthermoe, it is diduced as a another reason that the counterflow velocity induce by the compression shock cause the fluctuation. However, it is still an open question and more detailed experiments are needed to investigate the problem.

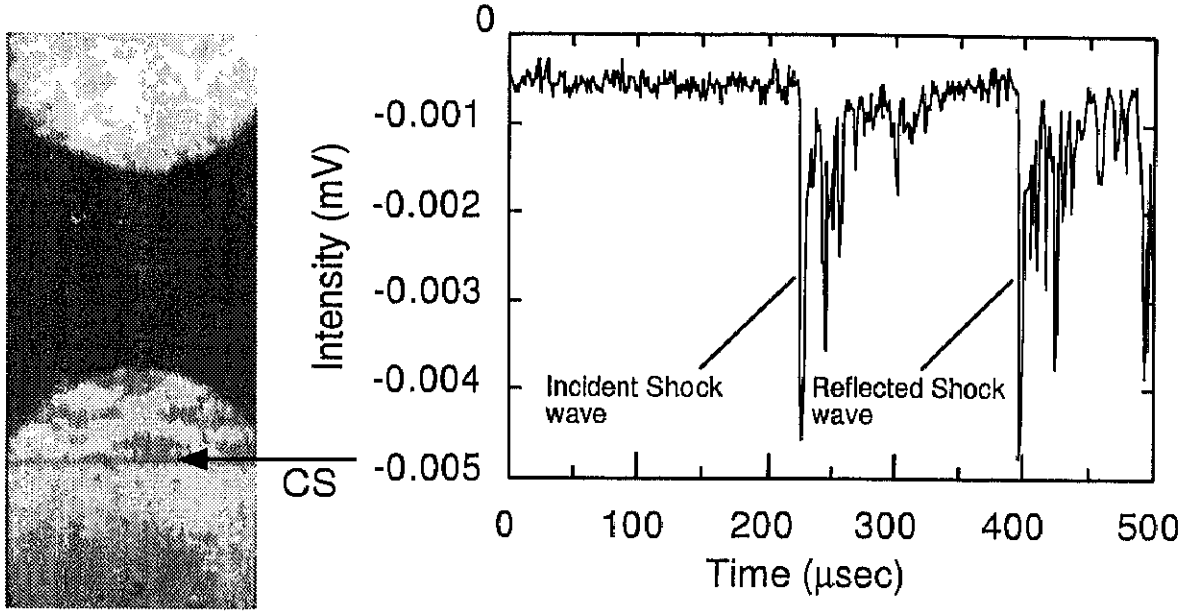


(a) He II

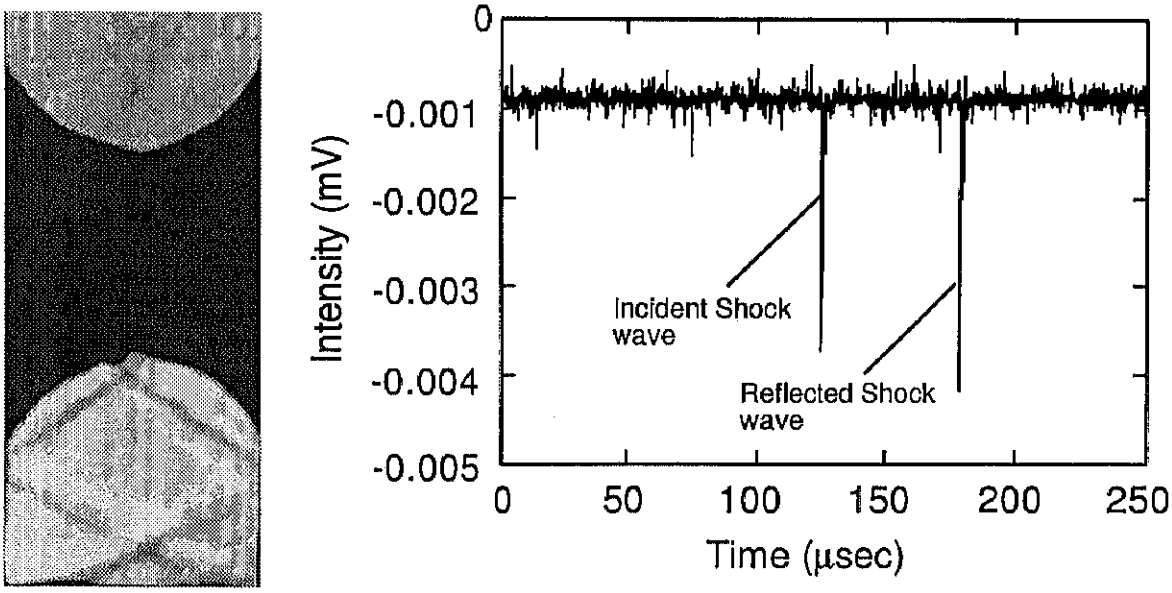


(b) Liquid nitrogen

Figure 5.19: Time variations of intensity of laser beam transmission and visualization photographs of transmitted compression shock wave in; (a) liquid nitrogen:$p_1 = 24.6\ kPa(68\ K)$ (b) $HeII$:$p_1 = 2.8\ kPa(2.0\ K)$

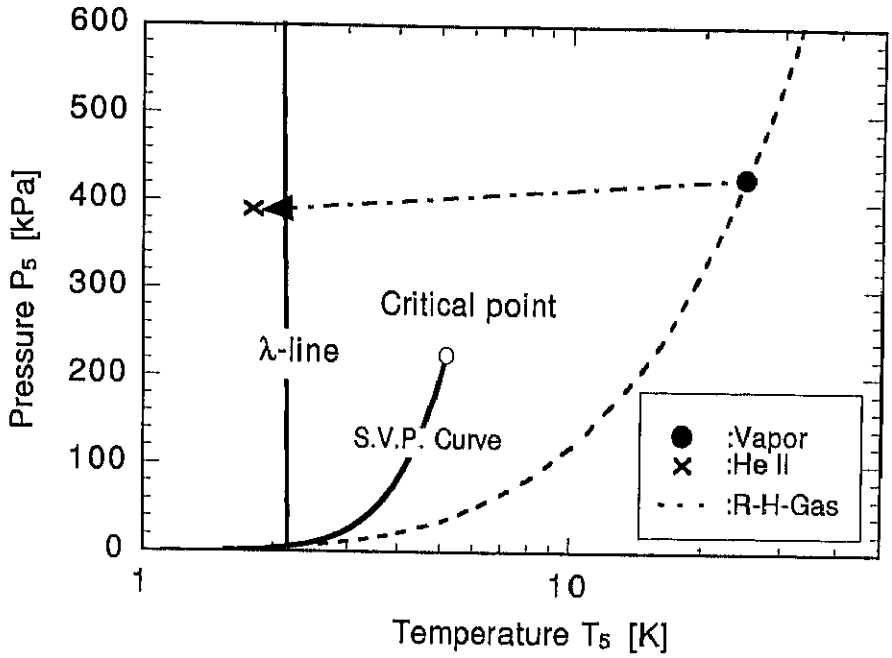


Figure 5.20: Thermodynamic state near *HeII* free surface. •:behind reflected vapor shock . ×:behind transmitted shock in *HeII*. The dotted line is *R-H-Gas* relation between $T_5$ and $p_5$ for 2.15 $K$.

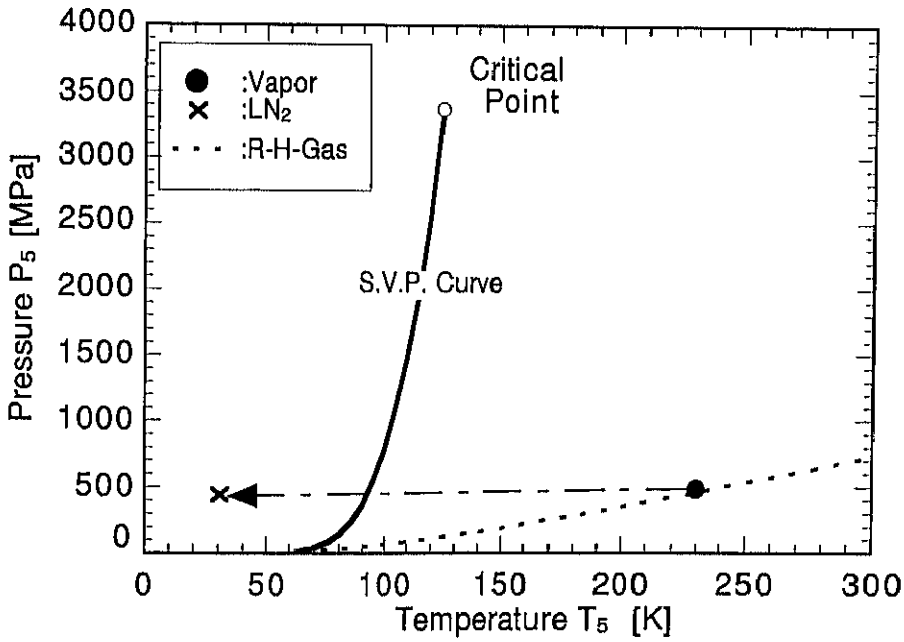


Figure 5.21: Thermodynamic state near liquid nitrogen free surface. •:behind reflected vapor shock. ×:behind transmitted shock in $LN_2$. The dotted line is *R-H-Gas* relation between $T_5$ and $p_5$ for 65 $K$.

### 5.3.5 Numerical solution for *R-H-HeII*

Calculation for compression shock waves in $HeII$ was made for six different initial temperature $T_1$ on the saturated vapor pressure. For each of these six cases, shock induced flow states were calculated using shock Mach number $M_{SL}$ as the independent parameter. The numerical method is written in Chapter 3(p 31). In this subsection, the numerical calculation result for a compression shock wave is only represented.
Eight plots were shown for each cases with the following notation.

1. Trajectories (final states on the $HeII$, $p$-$T$ diagram) are indicated by open circles for the numerical solution, and by the dotted line for the Khalatnikov approximation. And the isentropic curve for the isentropic process applied to liquid to helium is shown by the solid line, too.

2. The shock adiabatic (locus of final states on the $p$-$v$ diagram) is plotted as a solid line for the numerical solution Pressure change divided by initial pressure ($\Delta p/p_1$) is plotted on the vertical axis and specific volume change over initial specific volume ($\Delta v/v_1$) is plotted on the horizontal axis.

The remaining six plots show variation of a flow state variables with shock Mach number, $M_{SL}$ behind a shock wave. The variables plotted against $M_{SL}$ are:

1. Pressure jump $\Delta p$.

2. Temperature jump $\Delta T$.

3. Flow velocity $v$ behind a compression shock wave divided by first sound speed $a^*$ behind a shock.

4. Counterflow velocity $w$ behind a compression shock wave divided by first sound speed $a^*$ behind a shock.

5. Entropy jump $\Delta s$.

6. Entropy flux jump $\Delta \dot{s}$.

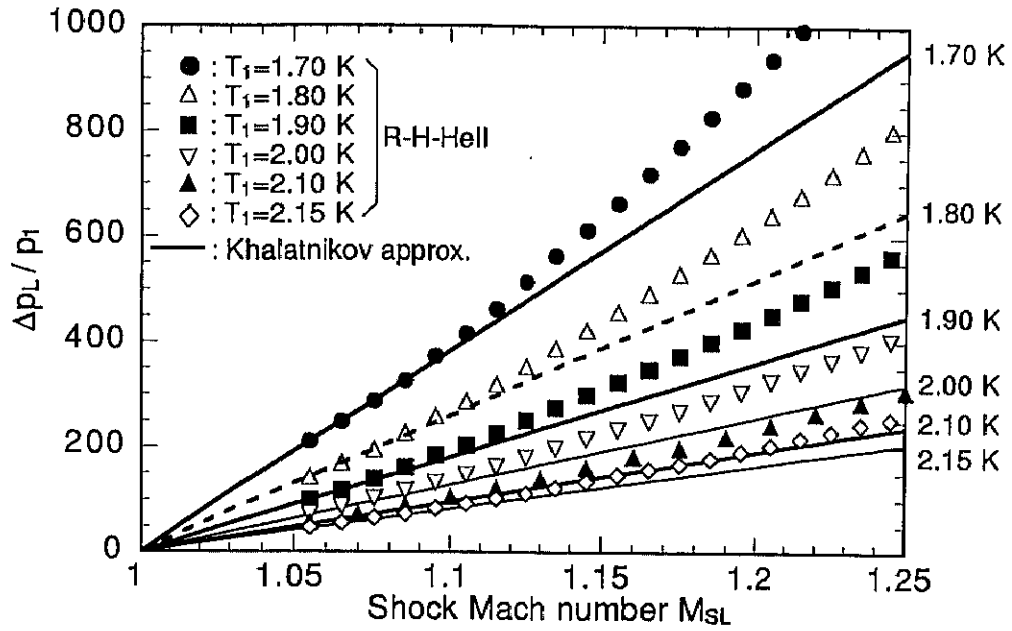


Figure 5.22: Pressure jump $\Delta p/p_1$ *vs.* shock Mach number $M_{SL}$.

Figure 5.22 through 5.22 show the results for compression shocks with initial state set at six initial temperature ($T_1 = 1.70\ K$, $1.80\ K$, $1.90\ K$, $2.00\ K$, $2.10\ K$, $2.15\ K$) on the saturated vapor pressure (*S.V.P.*). The pressure jump of a compression shock wave, $\Delta p/p_1$ is plotted against the shock Mach number $M_{SL}$ in Figure 5.22. The solid line is the Khalatnikov approximation and the dots are numerical solution calculated from *R-H-HeII* relation. The *R-H-HeII* relation and the Khalatnikov approximation coincide as they should as $M_{SL} \rightarrow 1$, but for higher Mach numbers the Khalatnikov approximation underestimates the numerically calculated pressure jump. The reason for this is that the non-linearity appears as $M_{SL}$ increases in compression shock waves in *HeII*.

Figure 5.23 shows the jump in temperature ($\Delta T/T_1$ *vs.* $M_{SL}$). While Khalatnikov approximate compression shocks in *HeII* as isothermal process,the full *R-H-HeII* relation indicates a temperature decrease, the magnitude of which increases as the wave strength increase.

Trajectories for the representative case are shown in Figure 5.24.The highest pressure final state for the *R-H-HeII* relation in the case of initial temperature of near the $\lambda$-temperature at $2.15\ K$ corresponds to $M_{SL} = 1.38$. Furthermore, in the case of initial temperature of $1.70\ K$, the numer-

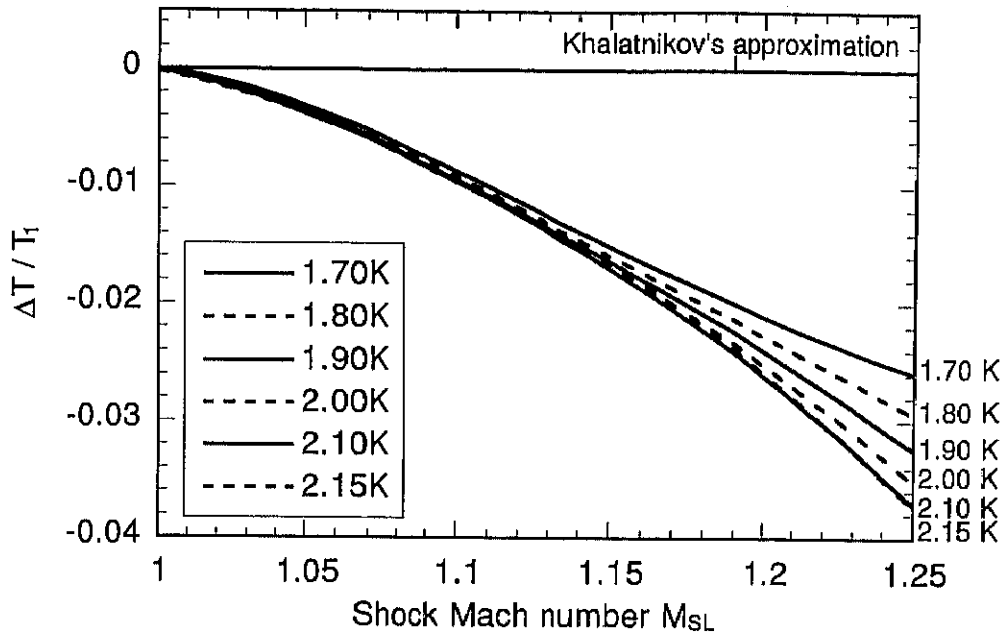


Figure 5.23: Temperature jump $\Delta T/T_1$ *vs.* shock Mach number $M_{SL}$.

ical calculation for *R-H-HeII* relation cannot be conducted if the shock Mach number $M_{SL}$ approaches at $M_{SL} = 1.40$. The reason for this is that the pressure behind a compression shock wave reaches to above 2.5 $MPa$ which is very close to the melting line and outside the range of *Hepak* thermodynamics database used here. That is to say, the state of behind a shock wave reaches to solid helium phase. Shock waves which convert liquid into solid helium are, of course, of great interest, but they are not considered here. Accordingly, the numerical calculation is conducted till the shock Mach number $M_{SL}$ is around 1.3 in this case, except for the initial temperatures $T_1$ =2.10 $K$ and 2.15 $K$. It is also of interest to note that shock Mach numbers $M_{SL}$, which are very modest by gasdynamic standards, produce very large pressure jumps in the liquid.

The shock adiabatic shown in Figure 5.25 is similar to the adiabatics seen frequently in gasdynamics. The slope is negative which is the only possibility in a classical material while the curvature is positive, indicating occurrence of compression shocks.

Figure 5.26 (5.28) and Figure 5.27 (5.29) show respectively the flow and counterflow velocities. Figures 5.26 and 5.27 show the normalized velocity behind a compression shock wave divided by first sound speed $a^*$ behind

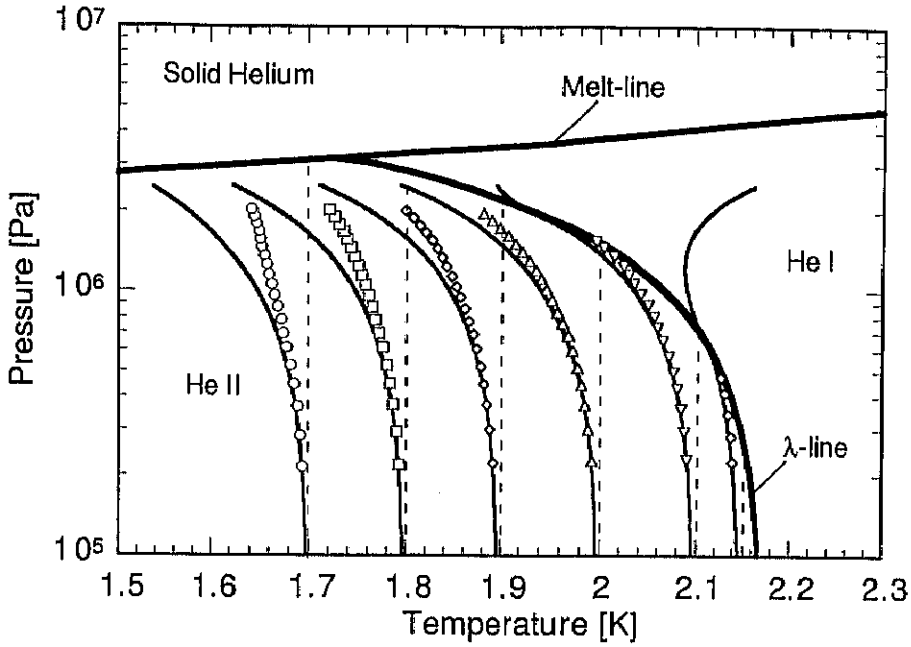


Figure 5.24: Shock adiabatic.

a shock. Figures 5.28 and 5.29 show only the velocity behind a compression shock wave divided by first sound speed $a^*$ behind a shock. Since the flow is compressed through the shock to a higher density, the flow velocity $v$ behind a shock jumps to ever lower (increasingly subsonic) values as the shock Mach number $M_{SL}$ increases. For the counterflow velocity $w$ produced by the compression shock, we see an interesting behavior. Within Khalatnikov's approximations, a compression pressure shock induces no counterflow, that is $w = 0$. However, the full *R-H-Gas* shows that $w$ is initially positive (away from the shock), goes through zero and becomes increasingly negative (toward the shock) for higher Mach numbers. This is more or less a general trend for all the compression shock cases which were calculated although the Mach number at which $w$ passes zero increases as the initial temperature $T_1$ increases on any given initial saturated vapor pressure. For those compression shock cases close to the $\lambda$-line, $w$ is always positive since before higher Mach numbers can be attached, the final state has crossed the $\lambda$-line.

In discussing entropy change across a shock wave in *HeII*, account must be taken of the transport of heat by convection with the normal fluid velocity $v_n$. For any general fluid flow through some fixed control volume $V$, the second law of thermodynamics can be expressed as a non-conservation

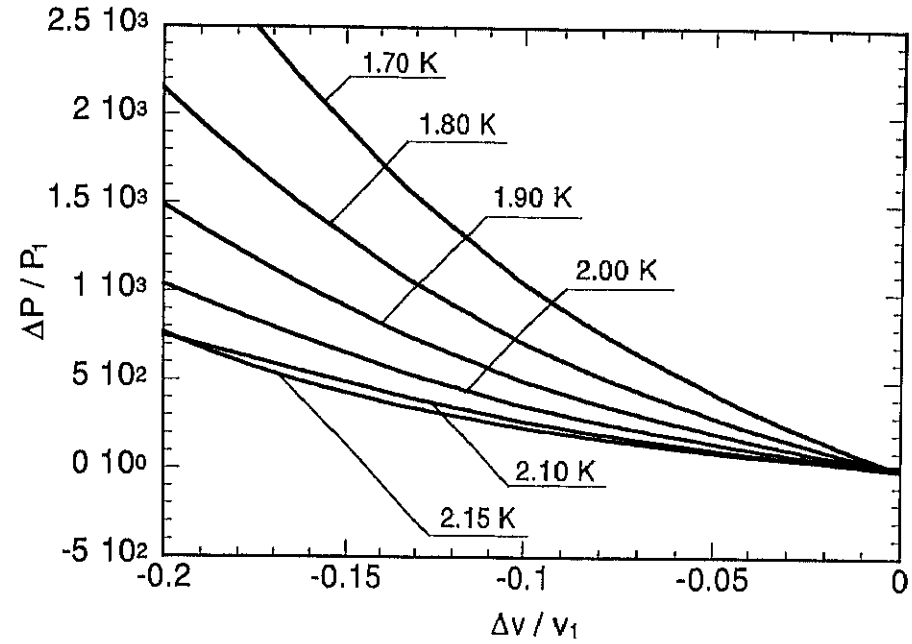


Figure 5.25: Hugoniot.

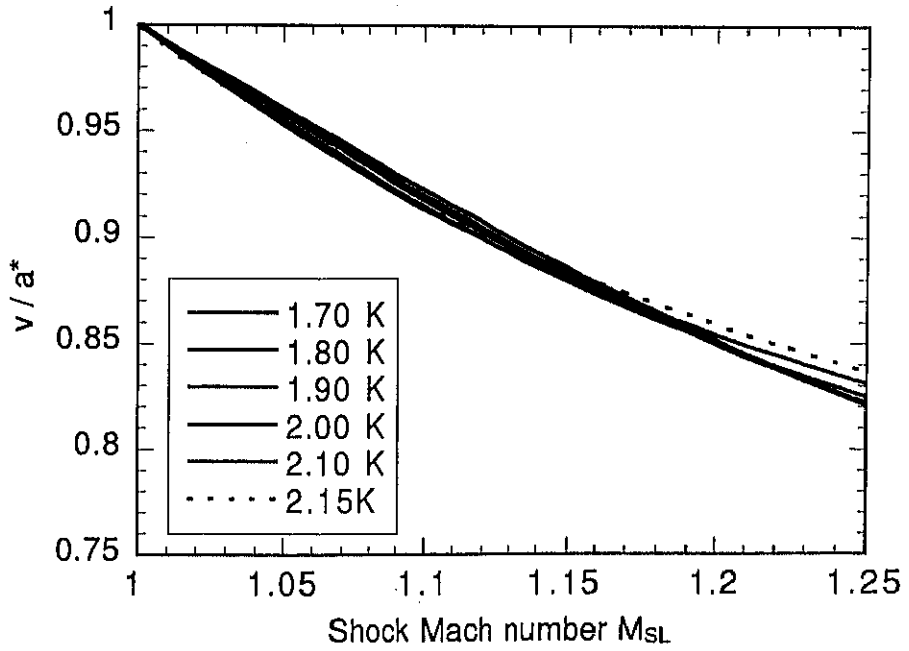


Figure 5.26: Normalized flow velocity $v/a^*$ behind a compression shock wave *vs.* shock Mach number $M_{SL}$.

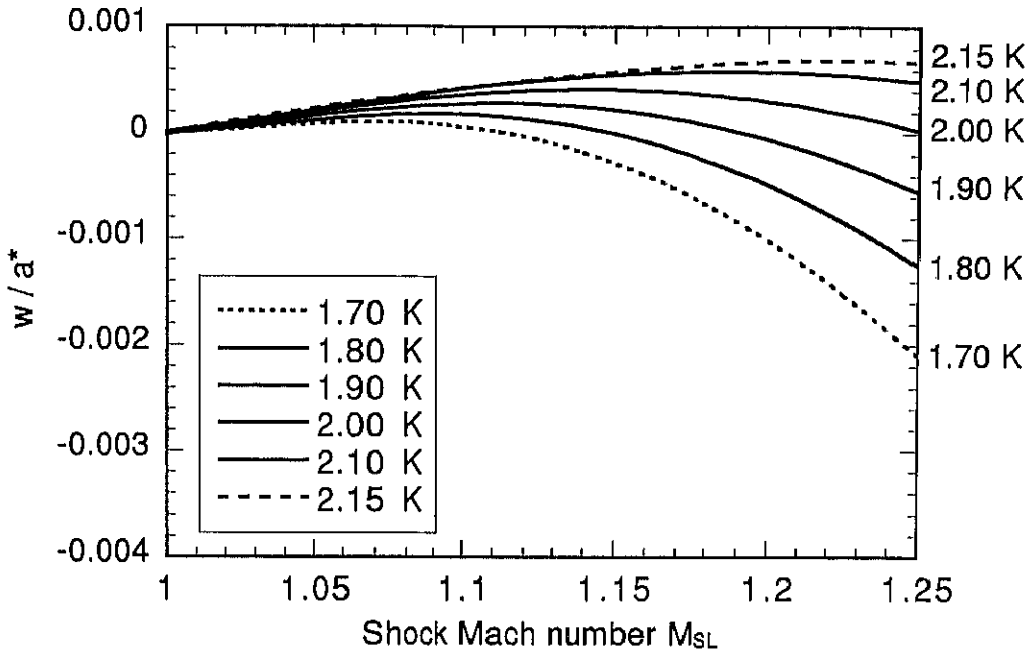


Figure 5.27: Normalized counterflow velocity $w/a^*$ behind a compression shock wave *vs.* shock Mach number $M_{SL}$.

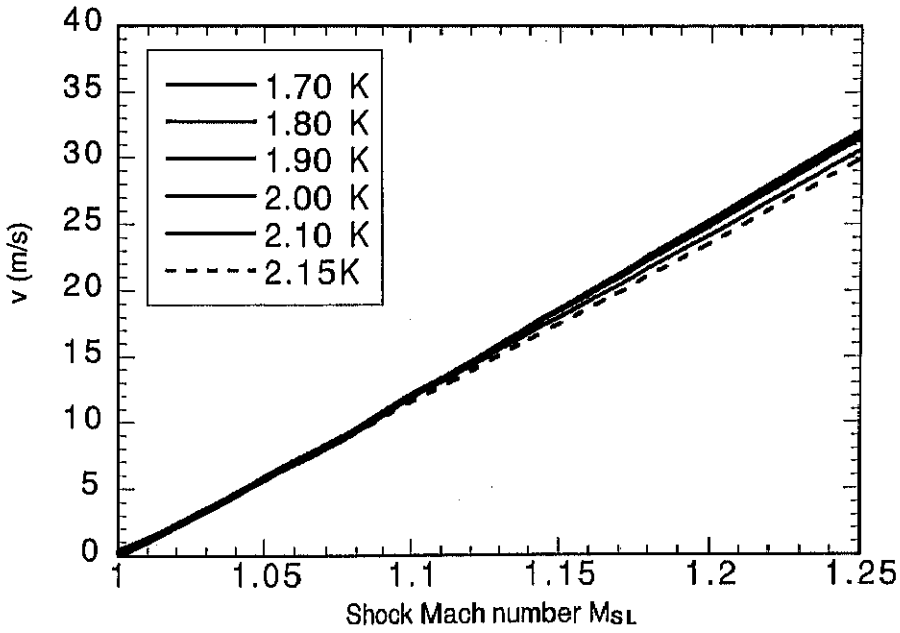


Figure 5.28: Flow velocity $v$ behind a compression shock wave *vs.* shock Mach number $M_{SL}$.

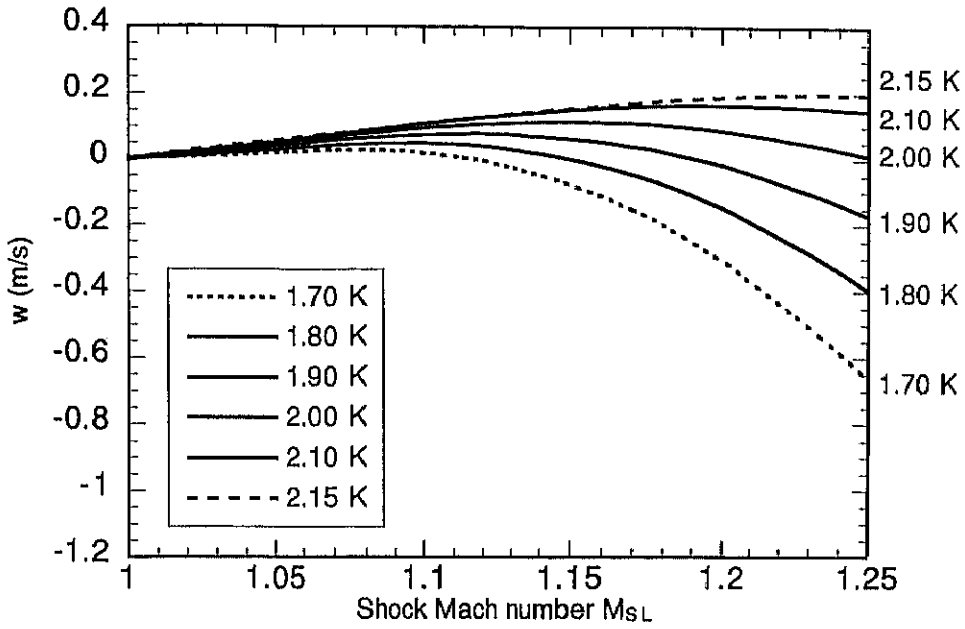


Figure 5.29: Counterflow velocity $w$ behind a compression shock wave *vs.* shock Mach number $M_{SL}$.

equation.

$$\frac{d}{dt}\int_V \rho s \, dV \geq -\int_A \frac{\mathbf{q}}{T} \cdot d\mathbf{A} \tag{5.1}$$

Here A is used for the closed surface bounding $V$, and the surface element normal vector is taken positive outward as is customary. The heat flux vector at the boundary is denoted by q and hence $\mathbf{q}/T$ represents the entropy flux $\dot{\mathbf{s}}$. In words, expression (5.1) states that the ratio of the entropy increase in $V$ exceeds or equals the entropy flux into $V$. Since all entropy in $HeII$ resides in the normal fluid fraction (§2.1.1, p 11) , heat flux in this liquid is given by

$$\mathbf{q} = \tilde{\rho}\tilde{s}T v_n \tag{5.2}$$

Applying equation (5.1) to the steady, one-dimensional flow through a fixed shock in $HeII$ gives the following:

$$\frac{q}{T} - \frac{q_1}{T_1} \geq 0 \tag{5.3}$$

or, denoting entropy flux by $\dot{s}$

$$\Delta \dot{s} \geq 0 \tag{5.4}$$

or, using equation (5.2) for $\mathbf{q}$

$$\tilde{\rho}\tilde{s}Tv_n - \rho_1 s_1 v_{n_1} \geq 0 \tag{5.5}$$

By using equation (2.1)(2.2)(2.3) to replace $v_n$ in favor of v and w, this becomes

$$\tilde{s}\left(\tilde{\rho}u + \rho_s w\right) - s_1\rho_1 u_1 \geq 0 \tag{5.6}$$

Conservation of mass as expressed by equation (2.49) can be used to write expressions (5.4) as

$$\frac{\tilde{s}}{s_1}\left(1 + \frac{\rho_s w}{\rho_1 v_1}\right) - 1 \geq 0 \tag{5.7}$$

Expression (5.7) is a generalization of the gasdynamic axiom: "Entropy must increase across a shock." This statement is a proper consequences of the second law of thermodynamics for the classical case where $w$=0. However, due to the presence of reversible, convective heat flux, the statement for *HeII* should be generalized to : "Entropy flux must increase across a shock." Positive $w$ indicates reversible extraction of heat from the flow behind the shock which results in the possibility of the entropy itself decreasing. The normalized changes in entropy $\Delta s/s_1$ and entropy flux $\Delta \dot{s}/s_1$ are shown for the representative pressure shock case in Figures 5.30 and 5.31, respectively.

Since the counterflow velocity, $w$, is much smaller than the velocity, $v_1$, the differences in the two plots (Figure 5.30 and 5.31) are insignificant. Such will not be the case for temperature shocks when $\rho_s w/\rho_1 v_1$ is large. From very general thermodynamic reasoning, the curve for change in entropy flux $\dot{s}$ should have zero slope and curvature as Ms $\rightarrow$ 1. That is, the entropy flux $\dot{s}$ change should be of order $(M_{SL} - 1)^3$ for very weak waves. (§ 2.77, p 24) From Figure 5.31, the solid line which represents the numerical solution

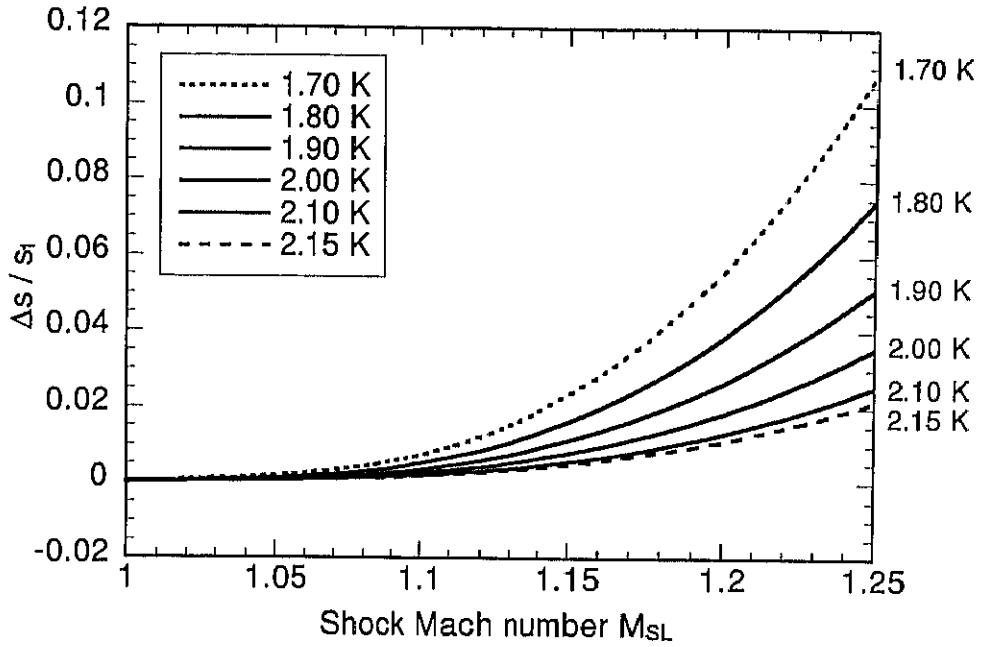


Figure 5.30: Entropy jump $\Delta s/s_1$ *vs.* shock Mach number $M_{SL}$.

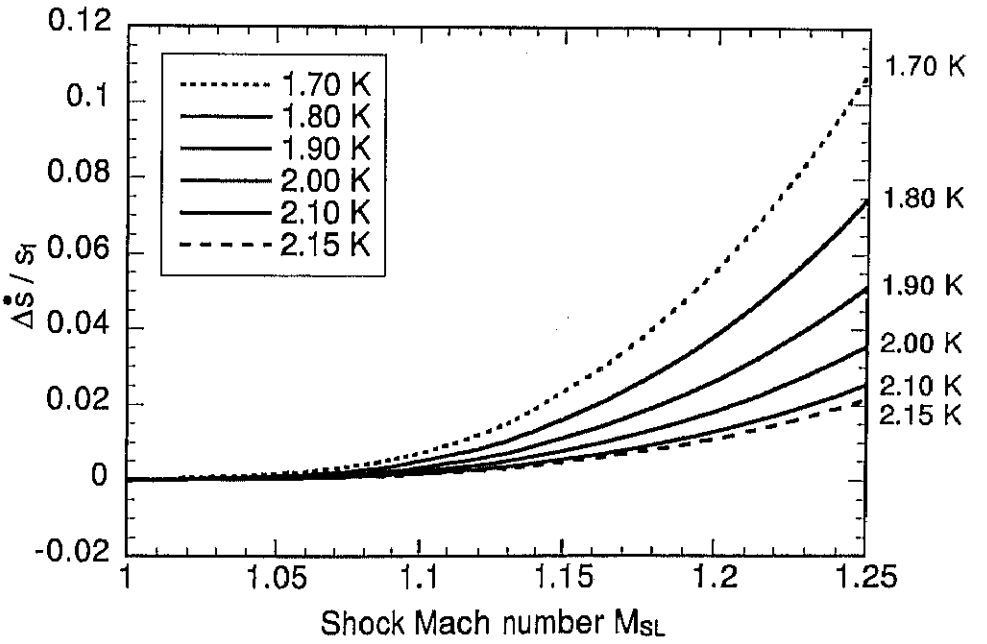


Figure 5.31: Entropy flux jump $\Delta\dot{s}/\dot{s}_1$ *vs.* shock Mach number $M_{SL}$.

fulfills these expectations. The plotted Khalatnikov entropy flux change (dashed line) obviously does not. The reason can be seen from examining the energy equation (2.51) rewritten below.

$$\tilde{\rho}\tilde{s}Tv_n + \rho_n v_n^2 w = \rho_1 s_1 T_1 v_{n_1} \tag{5.8}$$

According to Khalatnikov's approximations for compression shocks. $T = T_1$ and $w = 0$. Substituting these, together with continuity (2.49), and equation (2.1)(2.2)(2.3) gives simply

$$\tilde{s}\left(p, T_1, w = 0\right) = s_1\left(p_1, T_1\right) \tag{5.9}$$

Thus the energy equation is satisfied in the Khalatnikov compression shock approximation only if $\left(\frac{\partial s}{\partial p}\right)_T = 0$. This is equivalent to neglecting, the coefficient of thermal expansion $\beta$ since

$$\alpha = -\frac{1}{\rho}\left(\frac{\partial p}{\partial T}\right)_p = -\rho\left(\frac{\partial s}{\partial p}\right)_T \tag{5.10}$$

As mentioned before, the Khalatnikov formulas for the final state are arrived at by taking $\alpha = 0$. (§ 2.1.3, p 20) However, within the computer program, any final state regardless of whether it is calculated by the Khalatnikov approximation or found iteratively by Newton' method, is used as input to *Hepak* database to calculate all additional state variables (entropy, density, normal fluid fraction, etc.). Since $\alpha$ is in fact small and negative but not precisely zero in the true thermodynamics, the dashed lines on plots of secondary quantities (i.e., those which are not given explicitly in the six Khalatnikov approximation or taken to show the error which results from neglecting the coefficient of thermal expansion. For example, by equation (5.9), the dashed line in Figure 5.30 should be horizontal, but since $\alpha < 0$ the entropy will in fact increase with pressure indicated by the dashed line which is actually plotted.

## 5.4 Thermal Shock Wave in Superfluid Helium

A large number of studies have been conducted concerning a thermal shock wave in $HeII$. Our group also have been engaged in the researches on thermal shock wave relating phenomena, such as the propagation of a thermal shock wave and the deformation of wave forms by high density quantized vortices. In the conventional method of thermal shock wave generation by stepwise heating from a heater, the strength of a thermal shock wave is highly restricted because of boiling. So, the idea that the thermal shock wave is induced by a gasdynamic shock wave impingement is introduced in this study. Because there is no apparent limit of the heat flux to produce a thermal shock wave, it is expected that a thermal shock wave with strong non-linearity can be generated. And the interaction of both shock waves are possible to be caused. The thermal shock wave in $HeII$ is investigated by measuring the temperature variation with a superconductive temperature sensor and with the aid of the Schlieren visualization method.

### 5.4.1 Typical profile of thermal shock wave

Shown in Figure 5.32 is the transient record of the temperature variation $\Delta T$ detected by the superconductive temperature sensor in $HeII$. The first and second stepwise temperature drops (a), (b) result from the arrivals of a compression shock and a reflected one from the bottom. The third small temperature rise (c) is caused by a rarefaction wave generated upon reflection from a free surface.

The thermal shock wave (d), seen as a large positive temperature peak as large as about 130 $mK$, is generated by heating of $HeII$ free surface from compressed high temperature vapor upon the impingement of a gasdynamic shock wave. By comparing the wave forms of thermal shock wave generated in different manners, one example is a thermal shock wave generated by stepwise strong heating from a planar heater in $HeII$ shown in Figure 5.33. It is reported that in this experimental situation the profile of thermal shock wave is reduced to a limiting profile. In the case of strong heating from a planar heater, a second sound pulse is drastically deformed by strong interaction with quantized vortices and is reduced to a unique quite short triangular profile called the limiting profile. The profile of thermal shock

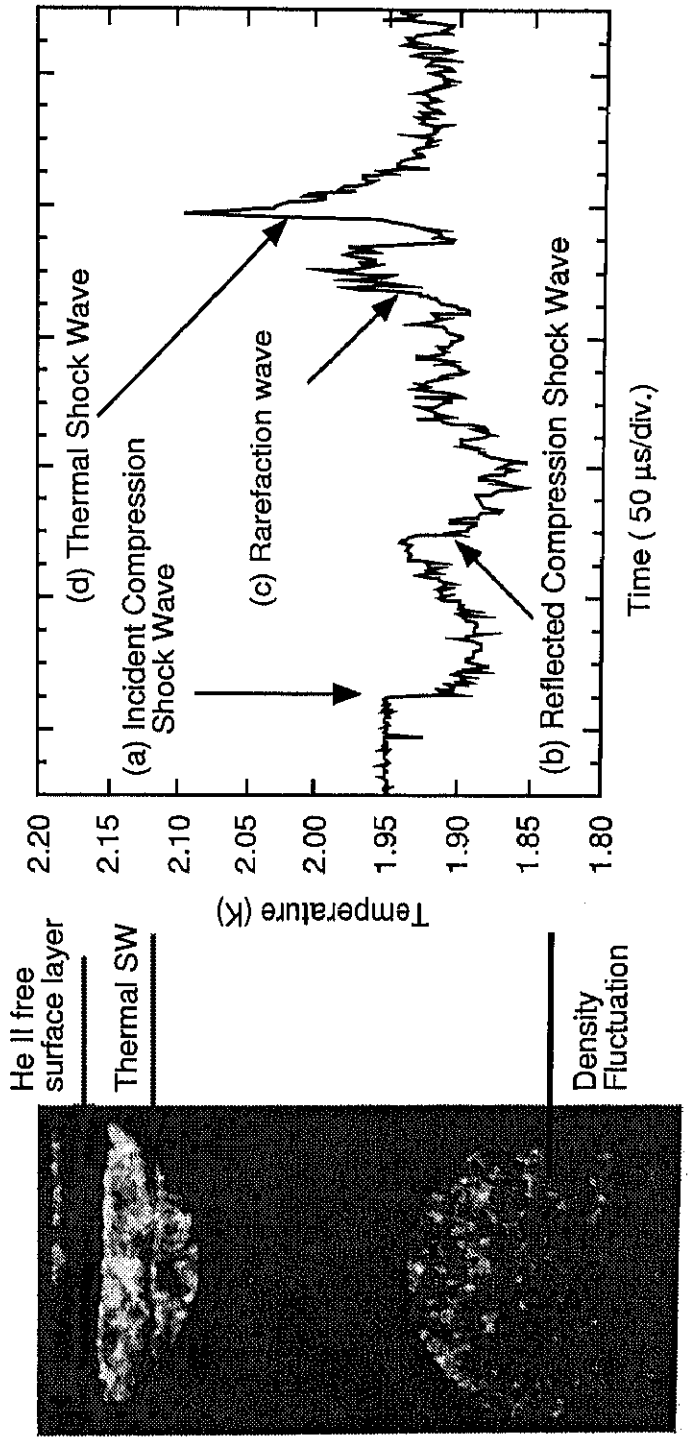


Figure 5.32: The transient record of the temperature variation $\Delta T$ detected by the superconductive temperature sensor in $HeII$. Driver gas; $p_4 = 500\ kPa$ (300 $K$), driven gas; saturated vapor of $HeII$, $p_1 = 2.77\ kPa$ ($T_1 = 1.95\ K$), $p_{41}$ ( $= p_4/p_1$ ) $= 180$. Transmitted shock speed in $HeII$ $U_{SL} = 249\ 4\ m/s$. Transmitted shock Mach number in $HeII$ $M_{SL} =$ 1.09. (a) transmitted compression shock wave, (b) reflected compression shock wave, (c) rarefaction wave, (d) thermal shock wave

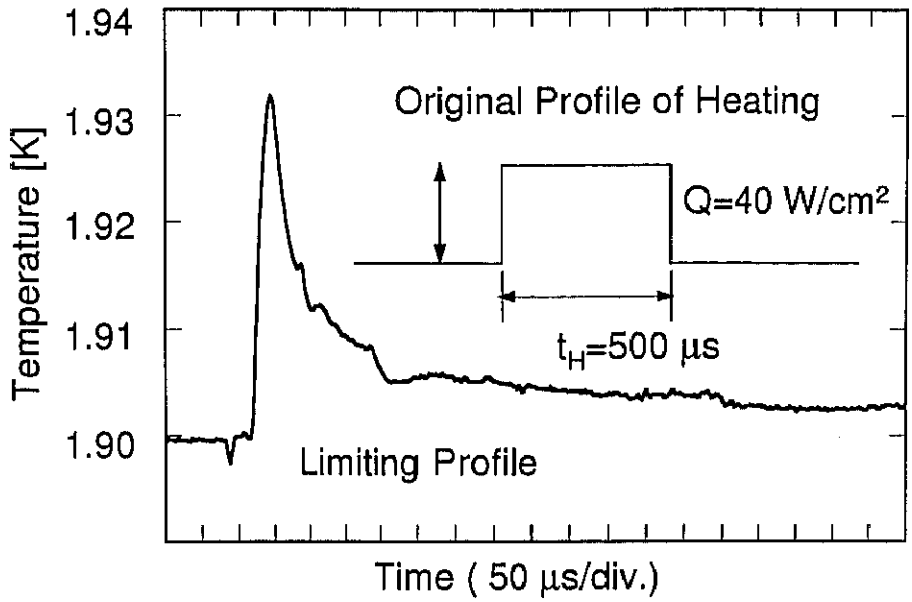


Figure 5.33: Temperature variation caused by stepwise heating in $HeII$; a limiting profile. $T_1$= 1.90 $K$, $Q$ = 40 $W/cm^2$, Heating time $t_H$ = 500 $\mu$ s $Q$: Input heat flux

wave generated in the superfluid shock tube is quite similar to the limiting profile. It is considered that the strong deformation in the present experimental result is also caused by the strong interaction with high density quantized vortices developed just below the free surface as illustrated in Figure 5.34. However, the amplitude is far larger than a limiting profile, of which peak was reported to be around 30 $mK$. The discrepancy may be reasoned as follows : The heat transfer from compressed high temperature vapor forming impinging gasdynamic shock wave to $HeII$ free surface may be far larger than 50 $W/cm^2$ which was the attainable maximum heat flux in the heating experiment. Second, the develop rate of quantized vortices, which are directly responsible to thermal energy dissipation to cause large wave form deformation forming a limiting profile, may be different in such pressurized state from that in saturated vapor pressure condition. However, it is still an open question and more detailed experiments are needed to investigate the problem.

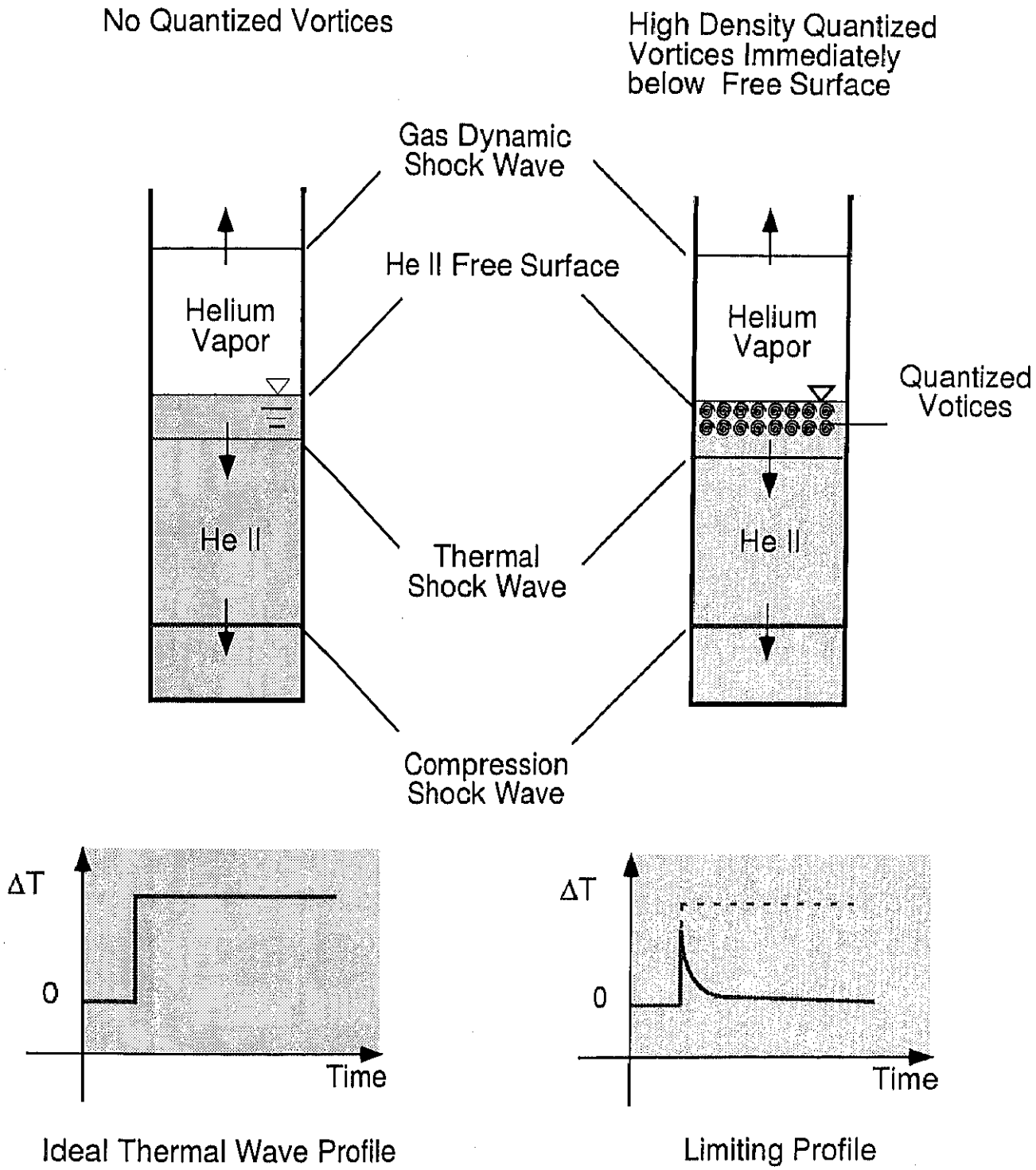


Figure 5.34: Schematic illustration of appearance of limiting profile.

### 5.4.2 Amplitude of thermal shock wave

Figure 5.35 shows the temperature amplitude of thermal shock wave which may be regarded as the shock strength of thermal shock wave plotted against the pressure jump appeared in corresponding transmitted compression shock for two initial temperatures 2.00 $K$ and 2.14 $K$. The pressure jump $\Delta p$ in this experiment corresponds to the heat flux in the case of strong heating experiment from a planar heater. It should be noted that the present thermal shock wave is not induced by the pressure jump due to the impingement of the gasdynamic shock but is generated by heating of $HeII$ free surface from compressed high temperature vapor upon the impingement of a gasdynamic shock wave. The pressure jump $\Delta p$ associated with the thermal shock wave can be neglected as it is very small compared with that of the transmitted compression shock wave. It is seen that the strength increases almost linearly with the pressure jump $\Delta p$ in the case of 2.00 $K$, although the wave profile of the thermal shock is quite similar to the limiting profile. However, in the case of initial temperature near the $\lambda$-temperature, 2.14 $K$, the $\lambda$-phase transition occurs when the pressure jump exceeds the pressure around 0.3 $MPa$, in which cases the thermal shock wave disappears.

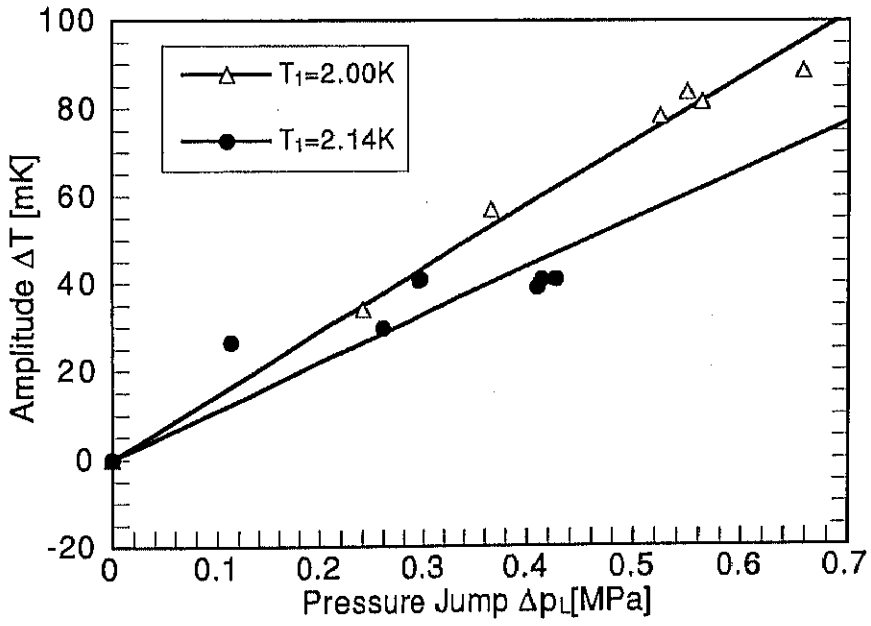


Figure 5.35: The amplitude of thermal shock wave $DeltaT$ as a function of pressure jump of transmitted compression shock wave $\Delta p_L$.

In this method of thermal shock wave generation by a gasdynamic shock wave impingement, the thermal shock wave with large amplitude can be generated.

### 5.4.3 Occurrence of thermal shock wave

Figure 5.36 shows a number of transient records of the temperature variation as the result of shock wave propagations in $HeII$ measured at various distances from the $HeII$ free surface. These data are not provided from a single shot of the experiment but are composed of those of several independent shots. The data reproducibility is quite satisfactory. The straight line $(A)$ indicates the propagation of a transmitted compression shock wave with a propagation speed of about 230 $m/s$, and $(B)$ the propagation of a thermal shock wave with a speed of about 20 $m/s$. In each transient record, the first and the second stepwise temperature drops result from the arrivals of a compression shock and a reflected one from the bottom, respectively. Please note that in this data plot waves propagating from the free surface obey the $x$-$t$ relation for shock wave propagation, but the signals from the reflected waves from the shock tube bottom can not be arranged along straight lines, $x$-$t$ diagram because of rather random distance of the detector from the shock tube bottom for each shot. It is seen from the result in Figure 5.36 $(B)$ that the thermal shock wave is not generated at the moment when a gasdynamic shock impinges onto the $HeII$ free surface. It is of interesting to note that in this particular example the compressed free surface region where the temperature rises to about 40 $K$ according to the calculation from *R-H-Gas* relation in helium vapor turns to super critical state. Of course, the $HeII$ free surface that initially divides helium vapor from $HeII$ disappears in the case shown in Figure 5.36. And a region with a very large temperature gradient, called the thermal boundary layer hereafter, is formed across the original free surface. Figure 5.37 illustrates the physical model of the thermal boundary layer. As seen from the temperature variation in Figure 5.32 and the visualization photos in the thermal boundary layer extends to several $mm$ in thickness within a very short time. It consists of three thermodynamic states of helium, that is compressed vapor and compressed $HeII$, and compressed $HeI$ in-between. It is considered that in the thermal boundary layer thermal conduction is a dominant heat-transfer

process. However, such other heat transport mechanism as the piston effect may be effective to supply large amount of heat through the supercritical state towards $HeII$ to generate thermal shock wave. It is understood that the mechanism of the wave deformation with a limiting shock strength is the strong interference with high density quantized vortices which develops as a result of large heating.

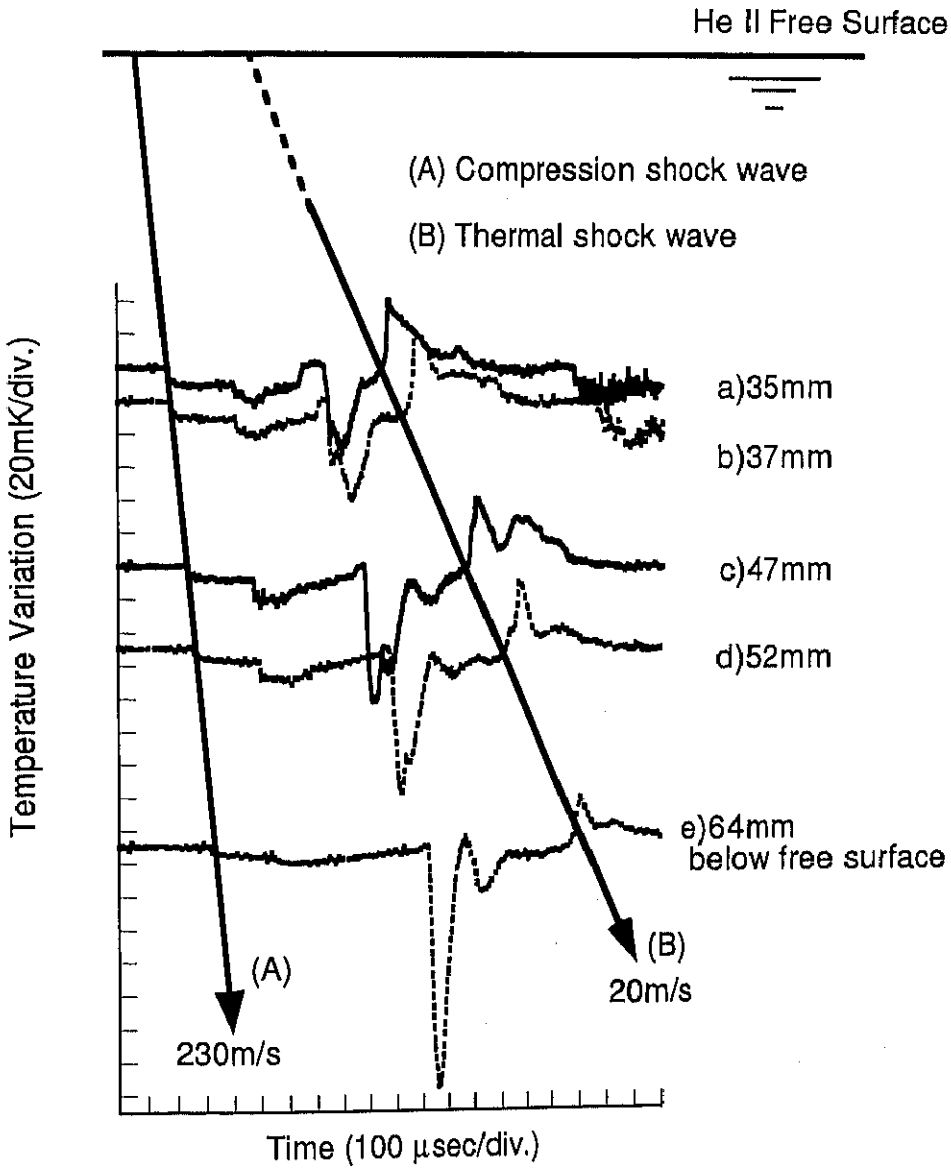


Figure 5.36: Time variations of the temperature resulting from compression shock waves and a thermal shock wave measured at five locations; (a) 35 $mm$ below free surface, (b) 37 $mm$, (c) 47 $mm$, (d) 52 $mm$, (e) 64 $mm$.

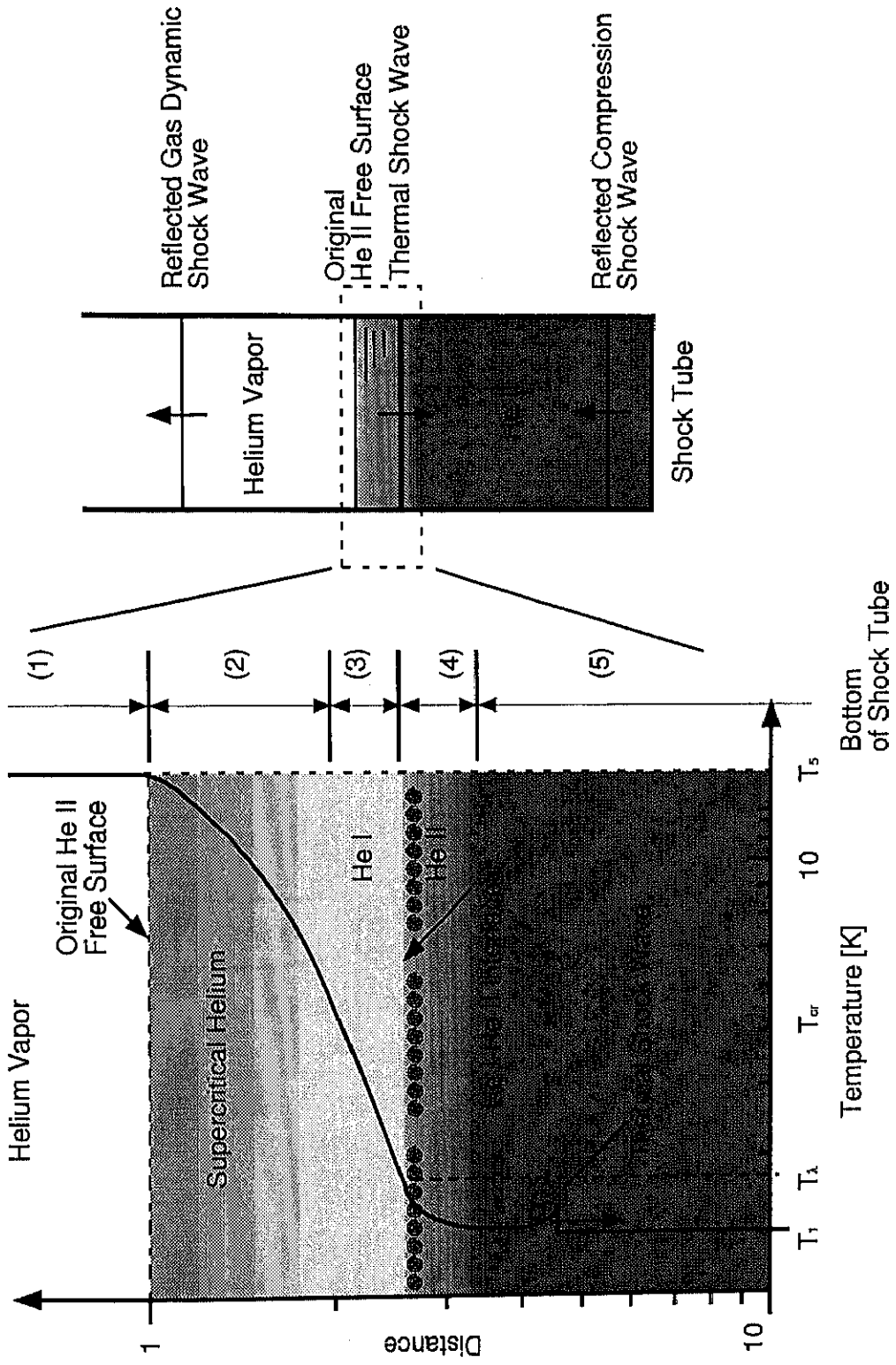


Figure 5.37: Thermal boundary layer induced by impingement of a compression shock wave on $HeII$ free surface. $T_1 = 2.00K$, $T_\lambda = 2.17\ K$, $T_{cr} = 5.20$ K, $T_5 = 40.0$ K. (1) compressed high temperature helium vapor region, (2) supercritical helium region (originally $HeII$), (3) compressed $HeI$ region (originally $HeII$), (4) high density quantized vortices region in $HeII$ (5) compressed $HeII$ region.

## 5.5 Highly Transient λ-Phase Transition

It is well known that two phases, *HeI* and *HeII*, exist in liquid helium shown in Figure 2.1. In engineering applications of subcooled (pressurized) *HeII*, the phase transition from *HeII* to *HeI* crossing the λ-transition line may appear prior to boiling and then the excellent cooling due to super-thermal-conduction of *HeII* would be lost. Accordingly, it is very important to understand the highly transient heat transfer in subcooled *HeII* accompanied by the λ-phase transition. Not a few studies have been carried out on the heat-transfer-induced-λ-transition, but none of them have paid attention to dynamic aspects of the process. Many studies of λ-phase transition have been made, mostly by (i) heating [54, 55], (ii) cooling [56 ~ 60] or a static pressurization of *HeII*, schematically indicated by processes (i) and (ii) in Figure 5.38.

*HeII* could be shock-compressed almost adiabatically to turn to *HeI* by crossing the λ-line in the case of *HeII* initially at temperatures rather close to the λ-temperature (process (iii) in Figure 5.38).

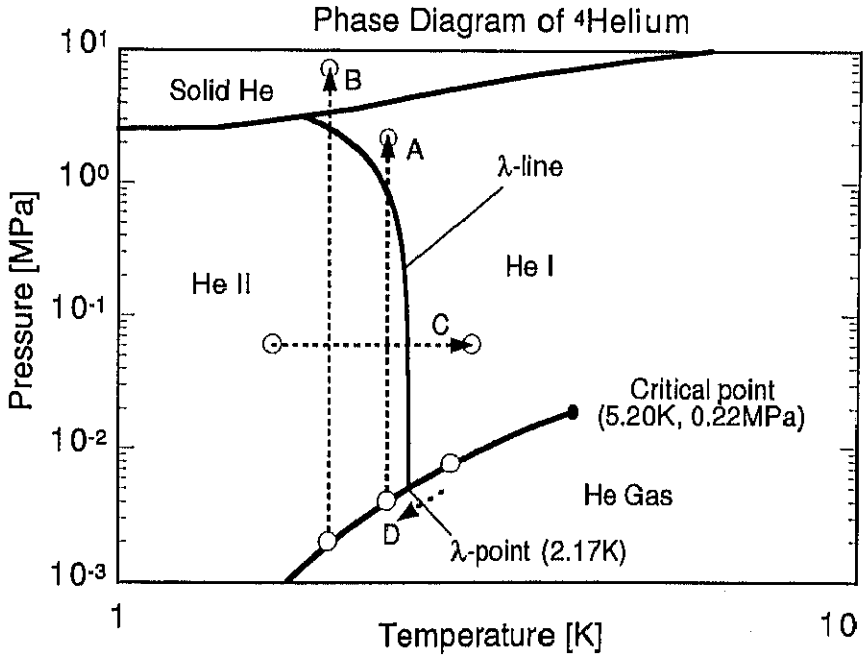


Figure 5.38: Schematic illustration of various methods due to phase transitions. A: λ-phase transition by shock compression. B: *HeII*-solid helium phase transition by shock compression. C: λ-phase transition by heating. D: λ-phase transition by cooling.

Furthermore a phase transition from $HeII$ to solid helium (quantum solidification) could be induced by shock compression up to a pressure higher than 2.5 $MPa$ (process (iv) in Figure 5.38) behind a reflected shock wave from a solid boundary where the mass velocity is zero. (Though this kind of phase transition, $HeII$ to solid helium, has not been tested yet, it is very interesting from the viewpoint of generation of a quantum solid in a highly transient process.) In this study, we cause $HeII$ to $HeI$ $\lambda$-phase transition by a sudden pressure rise as a result of shock compression (process (iii)) to investigate it from dynamic point of view. The process arising in the shock tube facility is an extremely high-speed one with a characteristic time of the order of a few $\mu$ sec and would be a non-equilibrium phase transition. This may be the first study on the highly transient $\lambda$-phase transition. The transient temperature variation was primarily investigated to confirm the occurrence $\lambda$-phase transition.

### 5.5.1 Temperature variation associated with $\lambda$-transition

Figure 5.39 shows three data records of temperature variations detected by the superconductive temperature sensor. The data of Figure 5.39 is the $HeII$ compression results without $\lambda$-phase transition, Figure 5.40 the $\lambda$-transition and Figure 5.41 is a special case with $\lambda$-transition. In the Figure 5.39, there are two sharp temperature drops induced by a transmitted and a reflected compression shock. These temperature drops caused by shock compression are natural consequence of the negative thermal expansion coefficient of $HeII$ that is a characteristic of $HeII$. This temperature variation indicates that the $HeII$ still remains $HeII$ after shock compression. The thermal shock wave is observed in the latter half of the data record in Figure 5.39. On the other hand, the trace in Figure 5.40 is the record of the $\lambda$-transition from $HeII$ to $HeI$ induced by shock compression, where the initial temperature $T_1$ is 2.16 $K$ which is rather close to the $\lambda$-temperature. In fact, this is the evidence that the $HeII$ converts to $HeI$ of which thermal expansion coefficient $\alpha$ is positive. It may be concluded that the $HeII$ converts to $HeI$ by crossing the $\lambda$-line due to shock compression without any appreciable time delay. Since a positive temperature jump appears from the beginning of the shock compression, it can be concluded that the $\lambda$-transition occurs in a relatively short time even under this highly transient

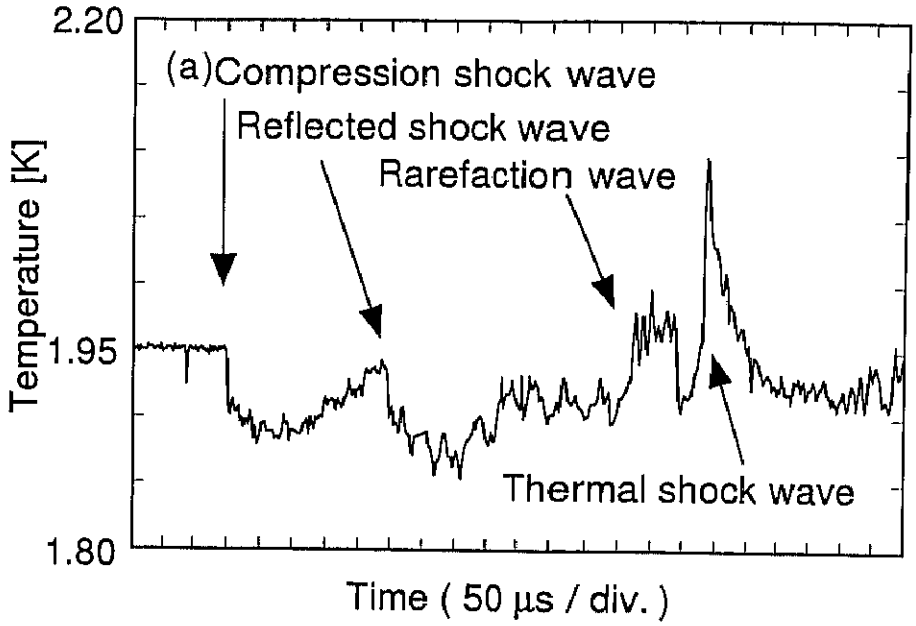


Figure 5.39: Transient record of the $HeII$ compression results without $\lambda$-phase transition. $T_1 = 1.95\ K$.

compression induced by the shock wave. Considering the fact that the $\lambda$-transition is a second order phase transition which does not involve latent heat, the actual occurrence of this highly transient phase transition may be quite reasonable. However, strictly speaking, the thermal expansion coefficient is still negative in the $HeI$ in a narrow temperature region around slightly higher temperatures than the $\lambda$-point as shown in Figure 5.42. Accordingly, one needs to confirm the non-existence of the second sound wave in order to verify the $HeII$ to $HeI$ $\lambda$-phase transition. In Figure 5.41, one sees a first negative jump and a subsequent positive jump in the temperature. This temperature variation suggests that the $HeII$ still remains $HeII$ after first compression by a transmitted compression shock and then converts to $HeI$ after further compression by a reflected shock from the shock tube bottom. No thermal shock wave is recognized in Figure 5.41 as well as in Figure 5.40.

The visualization photographs are shown in Figure 5.43 (a)-(d) for the case of initial temperatures of $T_1 = 2.10\ K$ and $2.16\ K$, respectively. In Figures 5.43 (a)-(c), a thermal shock wave is recognized near the $HeII$ free surface. The density variation associated with the thermal shock wave is very small compared with that caused by a compression shock. On the

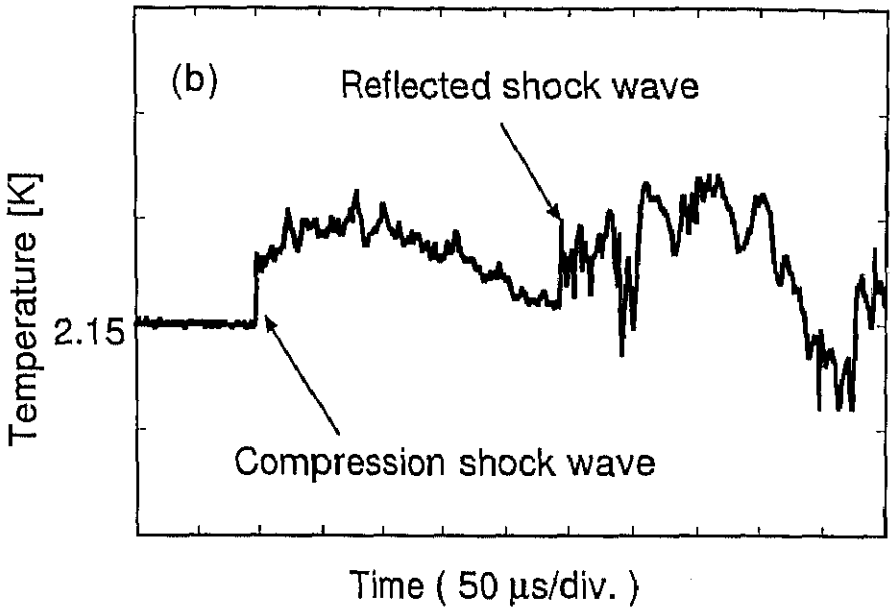


Figure 5.40: Transient record of the $\lambda$-transition from *HeII* to *HeI* induced by shock compression. $T_1 = 2.15\ K$.

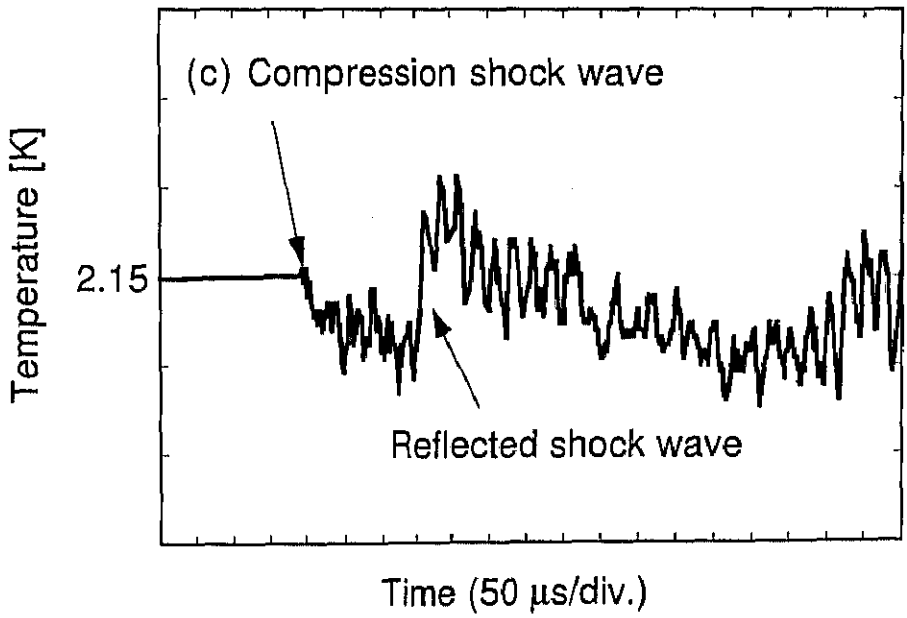


Figure 5.41: A special case with $\lambda$-transition.; from *HeII* to *HeI*, resulting from shock compression by reflected compression shock wave from the shock tube bottom. $T_1 = 2.15\ K$.

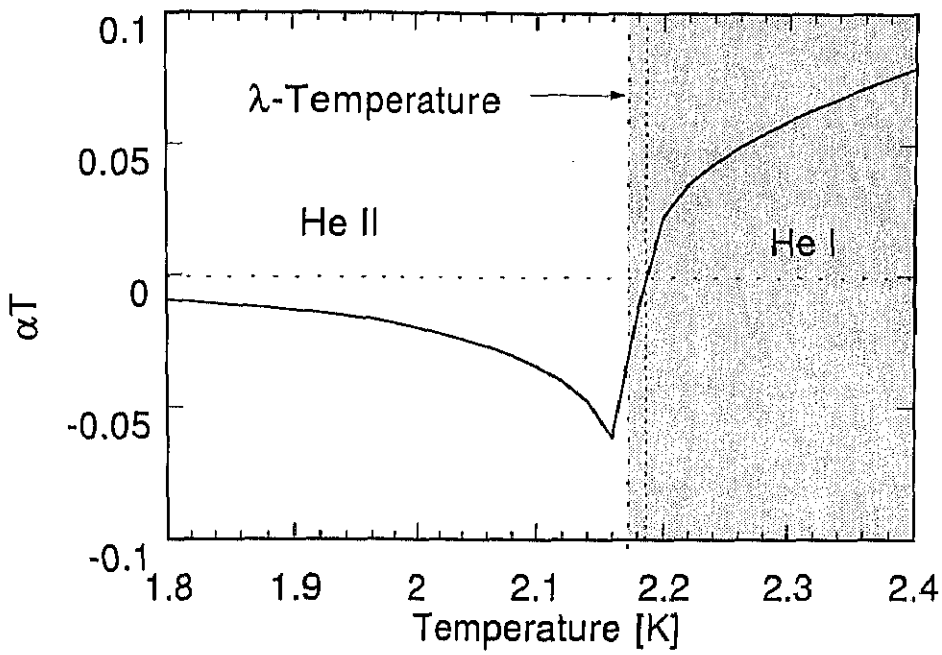


Figure 5.42: Thermal expansion coefficient of liquid helium, $\alpha$, along saturated vapor pressure. $\alpha$: Thermal expansion coefficient.

other hand, it is observed in these figures that the $HeII$ free surface zone becomes thick as time proceeds. Strong density fluctuations resulting from dynamic instability of the free surface and from anomalous behavior around the critical point may cause thickening of the free surface zone. In Figure 5.43 (d), no thermal shock is seen in the case of the initial temperature $T_1$ = 2.15 $K$. It is considered that a thermal shock wave is not excited due to the phase transition to $HeI$ in this case.

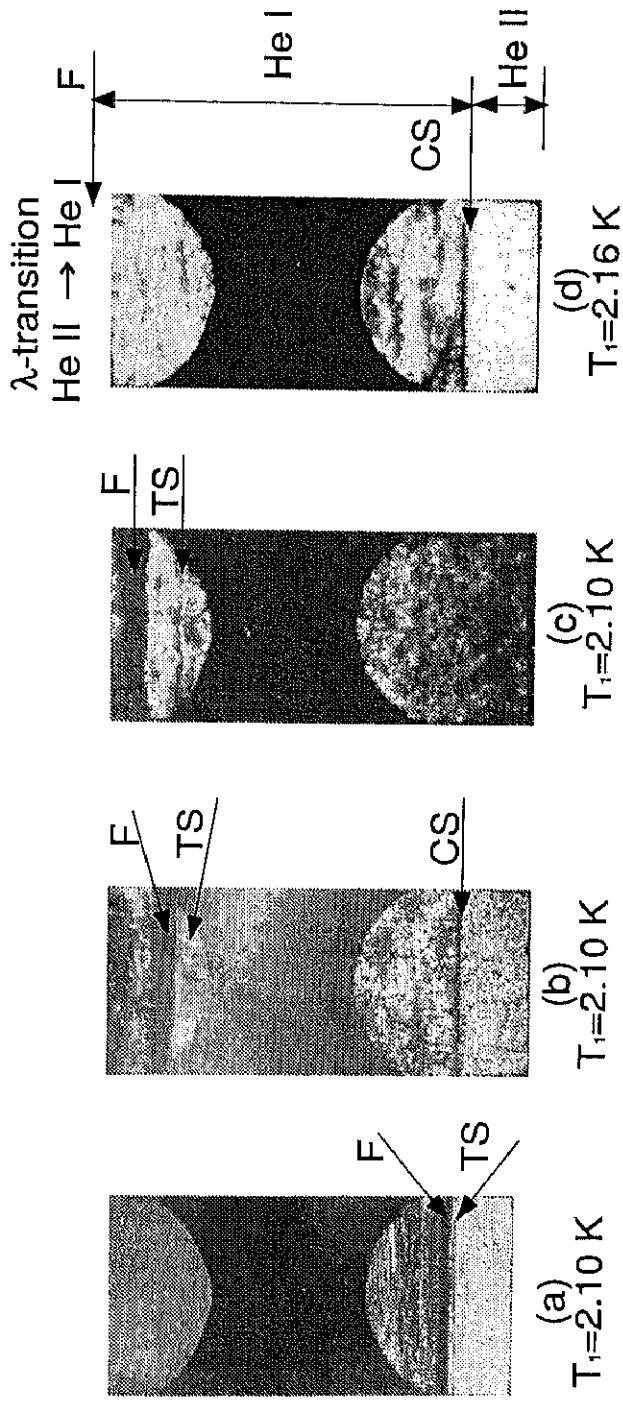


Figure 5.43: Visualization photographs of propagating thermal shock wave and *HeII-HeI* $\lambda$-transition. *F*: *HeII* free surface, *CS*: Transmitted compression shock wave, *TS*: Thermal shock wave. Thermal shock waves are located at; (a) 0.7 *mm* below *HeII* free surface, (b) 3.0 *mm*, (c) 6.8 *mm*, (d) *HeII-HeI* $\lambda$-transition, thermal shock is not excited.

### 5.5.2 Shock adiabatics in superfluid helium

The pressure and the temperature variations induced by transmitted shock wave in *HeII* are examined referring to the $p$-$T$ diagram given in Figure 5.44. The experimental data plotted together with shock adiabatics calculated from the *R-H-HeII* relation starting from four initial temperatures. And the isentropic curves are also given in Figure 5.44 for compression. Roughly speaking, compression causes a temperature drop in the *HeII*. It is found from this result that the temperature still drops as a result of shock compression within a narrow region adjacent to the $\lambda$-line even if *HeII* to *HeI* phase transition is induced. This results from the fact that the thermal expansion coefficient $\alpha$ is still negative in the narrow region near $\lambda$-line in *HeI* as shown in Figure 5.42. It is consequently seen that the $\lambda$-transition from *HeII* to *HeI* as the result of shock compression can not be confirmed only by a positive temperature jump. There is still a small possibility that the $\lambda$-transition

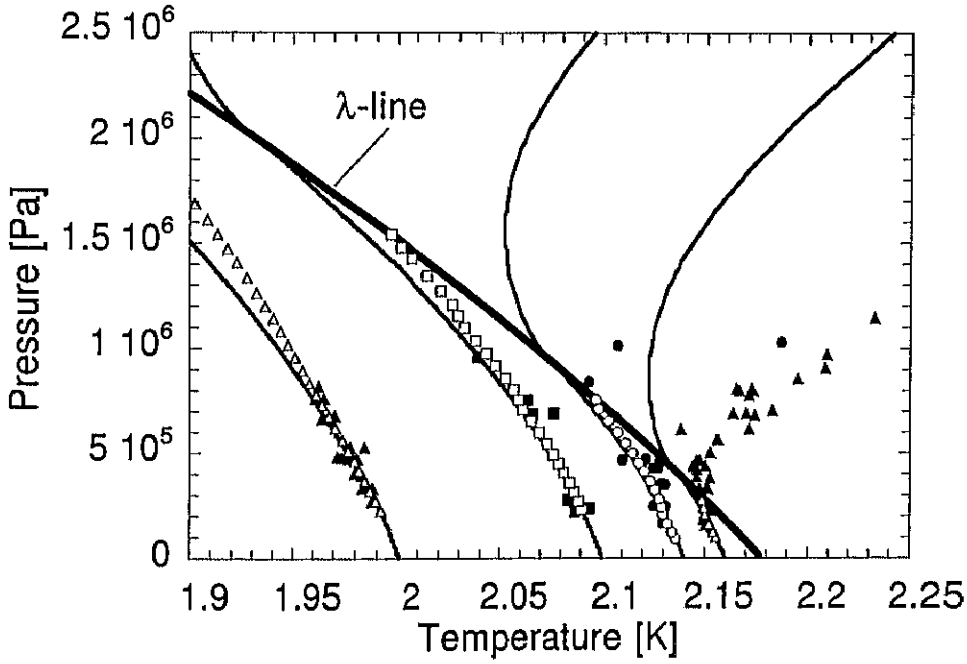


Figure 5.44: The temperature and pressure at the wave front of compression shock wave in *HeII* plotted for four initial temperatures of *HeII*. Solid lines are adiabatic curves (isentropic lines). Open circle are shock adiabatics. Closed circle are experimental data points.

from *HeII* to *HeI* leads to a negative temperature jump as mentioned above. Furthermore, the experimental data considerably deviates from the isentropic curve beyond the $\lambda$-line in the *HeI* region. In the shock compression process crossing the $\lambda$-line, the entropy is appreciable produced and thus the temperature rises significantly. The reason why such a large deviation from the adiabatic curve appears in this case is not yet wholly clear, though such aspect can be pointed out as the physical anomaly around the $\lambda$-line. Unfortunately, there is a small possibility that the calibration of the superconductive temperature sensor may not be accurate because of the difficulty in the calibration procedure in the trans-$\lambda$-line region. The heat transfer mechanism in *HeI* is different from that in *HeII*. In *HeII* the effective thermal conductivity is extremely large due to the superthermal conduction caused by internal convection mechanism, and thus the temperature of the sensor element can be regarded to essentially coincide with that of the surrounding *HeII*. However, the thermal conductivity of *HeI* is much smaller than the efficient thermal conductivity of *HeII*, and consequently, the temperature of the sensor element is, in general, higher than that of the surrounding *HeI*.